

Article

# Biosignatures in Subsurface Filamentous Fabrics (SFF) from the Deccan Volcanic Province, India

Jens Götze <sup>1,\*</sup>, Beda Hofmann <sup>2,3</sup>, Tomasz Machałowski <sup>4,5</sup> , Mikhail V. Tsurkan <sup>6</sup> ,  
Teofil Jesionowski <sup>4</sup> , Hermann Ehrlich <sup>5</sup>, Reinhard Kleeberg <sup>1</sup> and Berthold Ottens <sup>7</sup>

<sup>1</sup> Institute of Mineralogy, Technische Universität Bergakademie Freiberg, Brennhausgasse 14, D-09599 Freiberg, Germany; reinhard.kleeberg@mineral.tu-freiberg.de

<sup>2</sup> Natural History Museum Bern, Bernastrasse 15, CH-3005 Bern, Switzerland; beda.hofmann@geo.unibe.ch

<sup>3</sup> Institute of Geological Sciences, Baltzerstrasse 1+3, CH-3012 Bern, Switzerland

<sup>4</sup> Institute of Chemical Technology and Engineering, Poznan University of Technology, 60965 Poznan, Poland; tomasz.g.machalowski@doctorate.put.poznan.pl (T.M.); teofil.jesionowski@put.poznan.pl (T.J.)

<sup>5</sup> Institute of Electronics and Sensor Materials, Technische Universität Bergakademie Freiberg, D-09599 Freiberg, Germany; hermann.ehrlich@esm.tu-freiberg.de

<sup>6</sup> Max Bergmann Centre of Biomaterials, Leibniz Institute of Polymer Research Dresden, D-01069 Dresden, Germany; tsurkan@ipfdd.de

<sup>7</sup> Kalkofenstraße 15, D-96194 Walsdorf, Germany; ottens-mineralien@t-online.de

\* Correspondence: jens.goetze@mineral.tu-freiberg.de; Tel.: +49-3731-392638

Received: 26 March 2020; Accepted: 10 June 2020; Published: 16 June 2020



**Abstract:** The morphology, chemical, and mineralogical composition of subsurface filamentous fabrics (SFF) from the Deccan Volcanic Province (DVP) were investigated to determine the origin of these spectacular aggregates. SFF occur in a wide variety of morphologies ranging from pseudo-stalactites to irregular fabrics and are classified as SFF<sub>Ir</sub> (irregular) or SFF<sub>Ma</sub> (matted). The SFF samples exhibit a thread-like (or filament-like) center from which mineral precipitation starts to form the final macroscopic morphologies. Detailed investigations revealed organic material (fungal chitin) in the innermost filamentous core, which may have acted as an initial nucleus for the mineralization processes. The morphometric characteristics of certain filamentous fabrics are very similar to those of microbial filaments and the fabrics formed from them but are clearly distinct from similar types of non-biological precipitates (fibrous minerals, speleothems, and “chemical gardens”). These features indicate that the filamentous cores might be products of microbial communities that were active in the basaltic cavities. The SFF cross-sections display similar concentric layers of the mineral succession and reach thicknesses of several centimeters with spectacular lengths up to 100 cm and constant diameters. The typical mineralization sequence points to temporal variation in the chemical composition of the mineralizing fluids from Fe(Mg)-rich (Fe-oxides/-hydroxides, Fe-rich sheet silicates such as celadonite and di-/tri-smectite) to Ca-dominated (Ca-rich zeolites) and finally pure SiO<sub>2</sub> (opal-CT, chalcedony, and macro-crystalline quartz). Assuming biological activity at least during the early mineralization processes, circumneutral pH conditions and maximum temperatures of 100–120 °C were supposed. The formation of filamentous cores including Fe-bearing phyllosilicates probably occurred near the surface after cooling of the lava, where the elements necessary for mineral formation (i.e., Si, Mg, Al, Fe) were released during alteration of the volcanic host rocks by percolating fluids.

**Keywords:** subsurface filamentous fabrics; biosignatures; biomineralization; Deccan Volcanic Province; smectites; zeolites; silica minerals

## 1. Introduction

The Deccan Volcanic Province (DVP; Figure 1) is among the Earth's largest continental flood basalts and is known for its large euhedral crystals of zeolites and associated minerals. Often, well-developed crystals of these minerals occur on a substrate of subsurface filamentous fabrics (SFF), which exhibit easily recognizable forms of pseudo-stalactites (Figure 2). Hofmann [1] defined the term subsurface filamentous fabrics as microscopic to macroscopic mineral fabrics that result from the precipitation of minerals on a substrate of filamentous (thread-like) geometric units in subterranean environments.

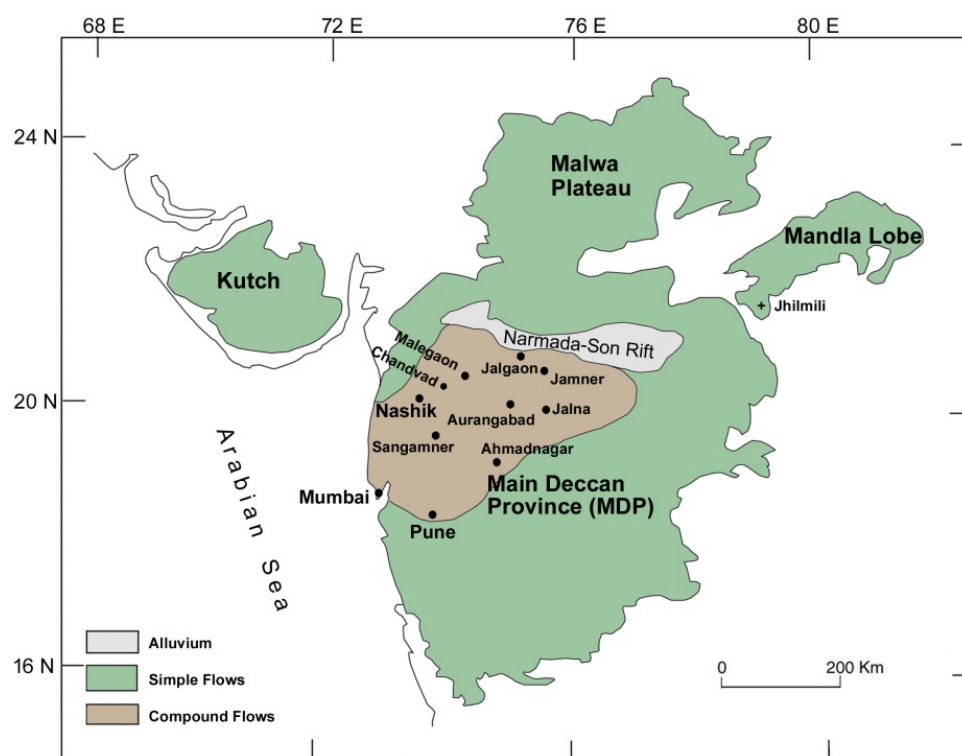


**Figure 1.** Map of the Deccan Volcanic Province (DVP) with the four main divisions and the most important sites of discovery of subsurface filamentous fabrics (SFF) occurrence in the compound lava flows of the Main Deccan Province (MDP).

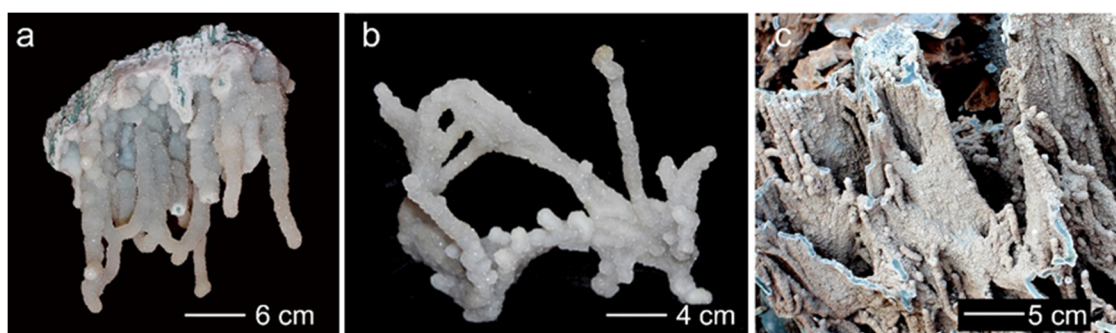


**Figure 2.** SFF from the MDP showing the basic morphological types: (a) straight and curved linear SFF<sub>Ir</sub> (irregular); (b) three-dimensional intergrowths of SFF<sub>Ir</sub>; (c) matted planar SFF<sub>Ma</sub>.

While the secondary minerals have been explored in detail [2–5], to date, the filamentous fabrics remain largely unnoticed, although they occur in a wide variety of morphologies and in remarkable sizes in large vesicles and cavities of compound lava flows in the central and northwestern parts of the Main Deccan Province (MDP; Figure 2).

Filamentous fabrics of similar size and with comparable variations in morphology are not reported from other large flood basalt provinces. So-called chalcedony-amethyst stalactites were found in the amethyst geodes of Artigas in Uruguay [6] and pseudo-stalactite aggregates were also reported in California, Mexico, and Brazil [7]. In addition, Hofmann et al. [8] described SFF of matted fabrics or irregular filaments from several basalts around the world. Their origin is still debated.

Since the formation of SFF in the MDP does not seem consistent with the classic speleothem-origin of stalactites, Ottens et al. [5] studied several representative specimens to obtain more detailed information about their genesis. As a result of these investigations it was concluded that the formation of SFF is probably related to processes of bio-mineralization rather than stalactitic growth or processes of self-organization.

The present study is focused on the morphology, macro- and micro-texture and chemical and mineralogical composition of the SFF from the DVP and aims to reveal the origin of these spectacular aggregates. Since the formation of SFF is intricately connected with the crystallization of certain secondary minerals in the basalt cavities, relevant aspects are partly included in the integrated study.

SFF from the DVP not only constitute a largely ignored substrate for spectacular mineral specimens of global significance, but they also represent impressive examples, often of significant size, of a poorly understood mineral formation process. The abundance of fresh exposures created by basalt mining in one of the world's best studied volcanic successions, combined with the interest in the associated spectacular minerals, make SFF from the DVP one of the most important and abundant examples of this type of mineral occurrence.

## 2. Geological Setting and Occurrence of SFF

### 2.1. Geological Setting

The Deccan Volcanic Province (DVP) is one of the largest continental flood basalt provinces (CFBs) [9,10], which are represented by voluminous basalt flows such as the Columbia River Basalt Group, the Paraná traps, and the North Atlantic Igneous Province. Most of the lavas erupted between 67.5 and 60.5 Ma and were fed by three main dyke swarms, namely (1) those trending N–S to NNW–SSE between the Arabian Sea and the Western Ghats; (2) those occurring along the Narmada-Satpura-Tapi region with an ENE–WSW strike; and (3) those located in a zone in the Western Ghats northeast of Mumbai, which have no preferred orientation [11–17]. Three stages of volcanic eruptions can be distinguished at around 67, 65 and 64 to 60 Ma, interrupted by two periods of quiescence lasting 2 Mio and 500,000 years, respectively [12,18–20]. Recent calculations by Sprain et al. [21] in the Western Ghats indicate that the main effusions took place with over 90% of the total volume between 65.4 and 66.4 Ma. It is believed that the Deccan volcanism is linked to widespread animal extinction at the K–Pg boundary (formerly K–T boundary) due to degassing of large amounts of CO<sub>2</sub> and SO<sub>2</sub> [15].

The DVP originally covered an area between 2,600,000 km<sup>2</sup> and 750,000 km<sup>2</sup> [22]. Nowadays the DVP basalts are distributed over an area of 500,000 km<sup>2</sup> and can be subdivided into four divisions: Main Deccan Province, Malwa Plateau, Mandla Lobe, and Kutch [22]. The paleo-thickness of the DVP is unknown, but it is assumed to have reached a maximum of around 3500 m in the Nashik area [22]. Large masses are eroded and the current maximum thickness near Nashik is about 2200 m.

The stratigraphy of the DVP is divided into three major subgroups: Kalsubai (2000 m thick), Lonavala (525 m thick), and Wai (1100 m thick), ordered from older to younger [23,24], as well as twelve formations. Each formation is characterized by accumulations of large composite sub-horizontal tholeiitic lava flows with varying thicknesses and chemical or mineralogical compositions. Based on these characteristics, simple and compound lava flows are generally distinguished [16,25]. Compound flows are abundant in the northwestern and central parts of the MDP (Figure 1) [26] within the estimated distribution of the Kalsubai subgroup [20].

The time between the eruptions of the two consecutive flows can vary widely, from hours, months, or years to thousands of years. Since age dating of such short time periods is not possible, the degree of

alteration of the surface zone plays an important indicator role. Surface weathering with a dependence on time and climatic conditions has resulted in more or less marked red or green alteration zones [22]. These horizons are not very pronounced in the investigated area of the MDP and indicate short interruptions of up to several years between the lava flows. Fossils or microfossils were not detected in the ancient surface zones of the MDP basalts.

The MDP consists of basalts without intercalated or overlaying sediment layers [27]. Moreover, investigations of the sub-trappean structure do not indicate noticeable sediments between the underlying crystalline Precambrian basement and the basalts [27]. Intertrappean sediments with records of fossils and paleoflora have not been found in the MDP, but were found at the boundaries of the DVP, for example, in the Salsette subgroup in Mumbai [28,29] and in Jhilmili [30,31].

## 2.2. Occurrence of SFF in the DVP

In the MDP, the SFF constitute an early formed assemblage of secondary minerals, such as phyllosilicates, zeolites, calcite, and SiO<sub>2</sub> minerals that have already been mentioned by Hofmann and Farmer [7] and Hofmann et al. [8]. Secondary minerals in basalts of the MDP were investigated by several researchers [2,32–35]. Ottens et al. [5] developed a model of secondary mineralization in three main stages, based on the mineralization in Jalgaon/Savda in the central DVP. In the first stage, clay minerals including the innermost SFF were formed near to the Earth's surface during the final cooling of the lava flows and incipient burial by following lava sequences. In a second stage, calcite, zeolites, and chalcedony crystallized due to low-grade metamorphism during burial. Minerals, such as heulandite, stilbite, powellite or apophyllite crystallized on chalcedony much later in the third stage at high temperatures (in Jalgaon/Savda up to 250 °C) from hydrothermal fluids.

For the first time, Ottens et al. [5] described SFF from specific outcrops in the MDP including complex fabrics of probably biogenic origin. Large aggregates of SFF of variable morphology, several centimeters long, were mainly found east of longitude 73°30' E in areas near Chandvad, Malegaon, and east of Sangamner as well as east of longitude 75°15' E around Aurangabad, Jalgaon, Jamner, and Jalna (Figure 1). The basalts of these areas belong mainly to the Kalsubai subgroup [21,36]. In contrast, long-term observations in the compound lavas of huge quarry complexes in Nashik, Pune, the New Bombay-Panvel area and in the spilite of Salsette Island, Mumbai could not confirm the presence of SFF west of longitude 73°30' E. This might be explained by the younger formations of the Lonavala and Wai subgroups or the latest eruptions of the Salsette subgroup. Moreover, SFF do not occur in the large units with dominant simple lava in the S–E part of the MDP, Malwa Plateau, Mandla Lobe, and Kutch due to the lack of vesicular basalts.

The SFF are commonly observed in vesicles and cavities (vesicles larger than 10 cm) in the cores of individual compound flows with a thickness of 5 to 10 m and occasionally in basaltic breccia. Individual lava flows, also named flow lobes, are bound either by contacts or weathered red or green bole horizons [37]. Bole horizons are weathered red-green-gray layers that mainly consist of clay minerals and were created as weathering products on the upper side of a basalt layer. In their composition they correspond to basalts rather than laterites. The units of a compound flow show a typical structure with a high-vesicular top, a rather dense core zone with a low number of large vesicles/cavities, and a bottom with upwards oriented pipe- or Y-shaped vesicles (e.g., [38]). The porosity within a lava flow depends on the size and arrangement of the bubbles [39]. In the upper zone, the lava solidified quickly resulting in small vesicles. In contrast, long-lasting high temperature and low viscosity of the lava in the central area causes coalescence of ascending bubbles and the formation of large cavities. The upper zone is characterized by high porosity and high permeability and is connected to the vesicles and cavities in the core zone by joints, caused by the shrinkage of the cooling lava. Figure 3 shows the characteristic zoned structure of a 7 m high quarry wall in Savda.

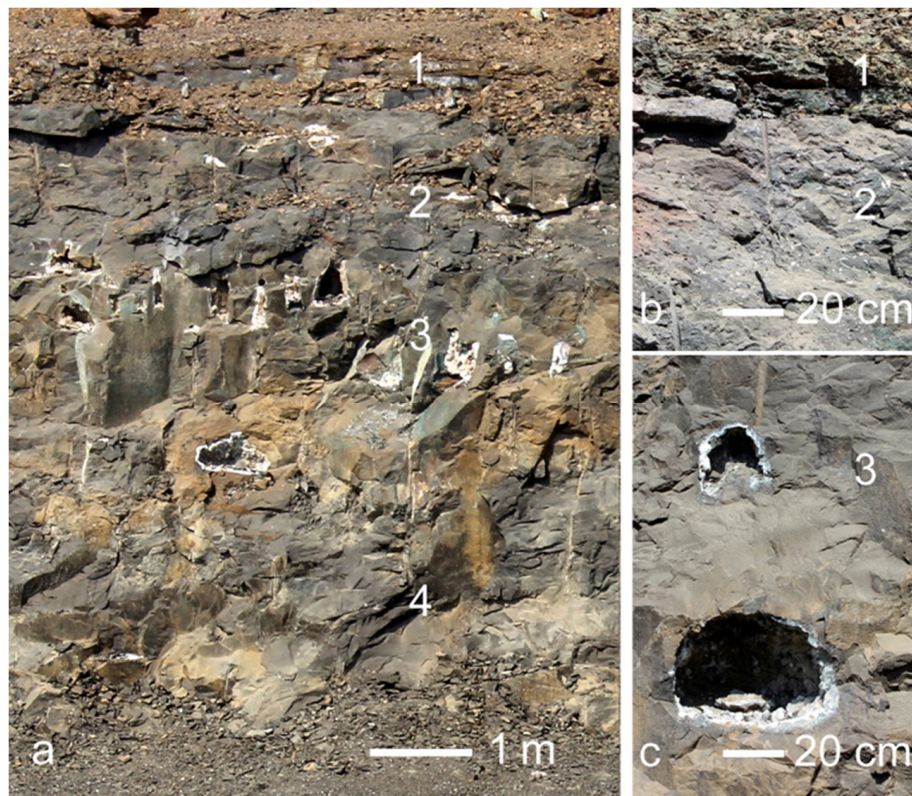


**Figure 3.** (a) Quarry wall (7 m high) displaying different zones: (1) bole; (2) intensely altered upper zone with large number of small vesicles, partly filled with secondary minerals; (3) dense flow core zone with large cavities; (4) bottom zone with a low number of vesicles. (b) Detail of an upper zone of a flow with (1) intensely weathered green bole; (2) intensely altered upper zone with high number of small vesicles, partly filled with secondary minerals. (c) Detail of the flow core zone showing dense host rock (3) with large mineral-lined cavities.

The photograph in Figure 4a shows a characteristic cavity from Jalgaon/Savda. The irregularly shaped cavity (40 cm wide) is hosted in the dense basalt of the flow core zone. A crust, a few millimeters to centimeters thick, of randomly intergrown SFF covers the cavity ceiling and walls. The SFF from the ceiling and wall partially show gravity-controlled elongation. A thick zone at the cavity bottom contains randomly intergrown SFF, completely embedded in chalcedony, similar to the so-called moss agate. The SFF consist of a green inner zone and a chalcedony crust of up to 1 cm.

In general, SFF from the MDP are easily recognizable as single filamentous fabrics, which form remarkable specimens in association with large euhedral crystals of secondary minerals, such as calcite, stilbite, heulandite, and apophyllite. It should be noted that SFF with a gravity-controlled orientation are conspicuous, but curved shapes, random intergrowths, and fully chalcedony-embedded formations (Figure 4b) are the predominant ones.

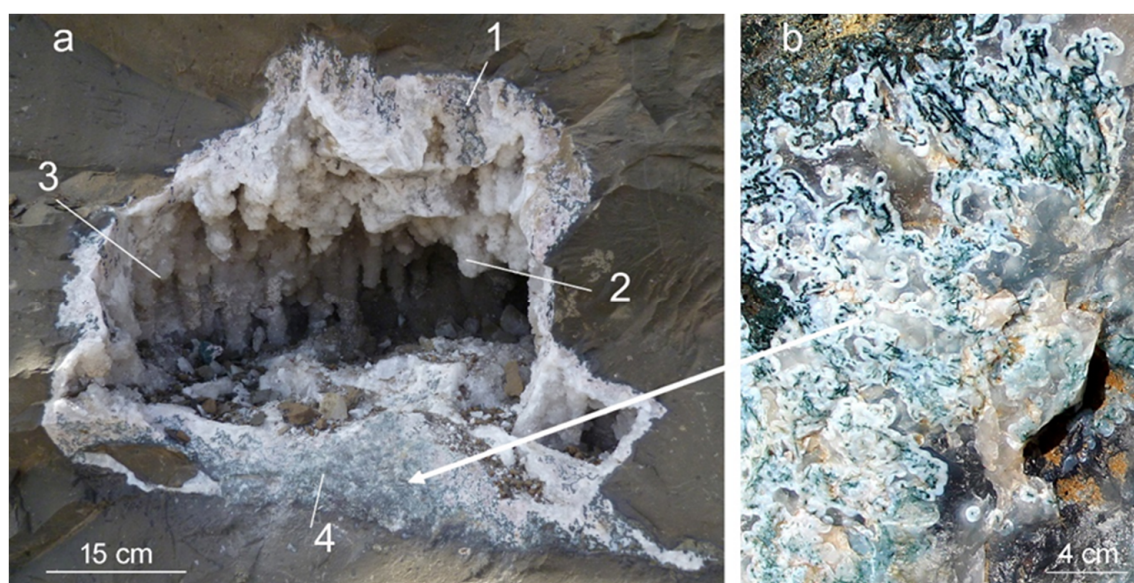


**Figure 4.** (a) Cavity from the flow core in Jalgaon/Savda representing SFF with variable morphology recognizable by the dark green color: (1) zone at the cavity ceiling with random intergrowths embedded in chalcedony; (2) linear SFF showing gravity-controlled growth from the cavity ceiling downwards into the free space; (3) side walls covered with random intergrowths and gravity controlled SFF; (4) cavity bottom with masses of irregular SFF embedded in chalcedony. (b) Close-up showing dark green filamentous structures embedded in chalcedony.

### 3. Materials and Methods

#### 3.1. Sample Material

Most of the sample material (SFF and secondary minerals) was collected during several field trips from large, freshly opened cavities within the flow core zone in the quarry complex of Savda near Jalgaon (Maharashtra, India; Figures 1–4). The huge quarry complex ( $20^{\circ}59' \text{ N}$ ,  $75^{\circ}27' \text{ E}$ , 230 m asl) contains countless numbers of small vesicles and large cavities in the basalt, which normally would not be of industrial interest. However, the cavities here contain a large number of valuable mineral specimens resulting in careful mining of crystals including SFF over the last 20 years. These mining activities allowed long-term observations and thorough geological and mineralogical studies of the SFF and related mineralization, which could be used for the present study.

Additional samples for comparison were selected from other outcrops in the surrounding MDP complex in the areas of Nashik ( $19^{\circ}53' \text{ N}$ ,  $73^{\circ}56' \text{ E}$ ), Chandvad ( $20^{\circ}20' \text{ N}$ ,  $74^{\circ}14' \text{ E}$ ), Malegaon ( $20^{\circ}33' \text{ N}$ ,  $74^{\circ}30' \text{ E}$ ), Jamner ( $20^{\circ}48' \text{ N}$ ,  $75^{\circ}46' \text{ E}$ ), Aurangabad ( $19^{\circ}52' \text{ N}$ ,  $75^{\circ}19' \text{ E}$ ), Jalna ( $19^{\circ}51' \text{ N}$ ,  $75^{\circ}54' \text{ E}$ ), and Sangamer ( $19^{\circ}31' \text{ N}$ ,  $74^{\circ}14' \text{ E}$ ) (Figure 1). Numerous field observations (between 1996 and 2016) and the careful evaluation of dozens of hand specimens provided information on the morphology and texture of the SFF and the mineralization sequence of the secondary minerals. Representative samples of different occurrences were selected for detailed analytical studies (Table 1).

**Table 1.** Investigated samples from the main volcanic province (India) showing the applied analytical techniques; (XRD = powder X-ray diffraction; SEM = scanning electron microscopy; EDX = energy dispersive X-ray analysis; SEMu-EDX = scanning electron microscopy of uncoated samples with local chemical by EDX; SEMc-EDX = SEM-EDX of carbon-coated samples; XRD = X-ray diffraction).

Sample No.	Sample Material	Locality	Figure	SEM	XRD	Morphometric Analysis	Bio-Analysis
Aur 02	Filament	Aurangabad			X	X	
Jal 01	Filament	Jalgaon		SEM <sub>u</sub>			
Jal 04	Filament	Jalgaon		SEM <sub>u</sub>			
Jal 05	Filament	Jalgaon	Figure 13	SEM <sub>c</sub> -EDX	X	X	
Jal 11	Filament	Jalgaon	Figure 11	SEM <sub>u</sub> SEM <sub>c</sub> -EDX			X
Jal 17	Filament	Jalgaon		SEM <sub>c</sub> -EDX		X	
Jal Sm 01	Filament	Jalgaon	Figure 14	SEM <sub>u</sub> -EDX SEM <sub>c</sub> -EDX	X		X
Jal Sm 03	Filament	Jalgaon		SEM <sub>u</sub> -EDX	X		
Jal 30	Cross-section Cavity wall	Jalgaon	Figure 7	SEM <sub>c</sub> -EDX	X		
Jal 31	Filament	Jalgaon	Figure 7	SEM <sub>c</sub> -EDX	X		
Jal 32	Filament	Jalgaon	Figure 10	SEM <sub>c</sub> -EDX			
Jal 33	Filament	Jalgaon	Figure 10	SEM <sub>c</sub> -EDX			
Jam 01	Filament	Jamner	Figure 16	SEM <sub>u</sub> -EDX SEM <sub>c</sub> -EDX	X		
Jam 10	Filament	Jamner	Figure 17	SEM <sub>c</sub> -EDX	X		
Jam 17	Filament	Jamner				X	
Jln 01	“Moss agate”	Jalna	Figure 18	SEM <sub>c</sub> -EDX		X	X
31226	“Moss agate”	Jalgaon				X	

“X” marks the analytical methods applied to the samples.

### 3.2. Analytical Methods

Macroscopic sample evaluation was followed by a careful examination using a ZEISS stereo microscope. In addition, polarizing microscopy in transmitted light on polished thin sections was performed on a ZEISS Axio Imager A1m microscope (ZEISS, Thornwood, NY, USA). The documentation of micro-textures in plane and crossed polarized light was realized using a digital camera AxioCam MRc5 (ZEISS microscopy, Jena, Germany) and the software Axiovision Rel. 4.6.

Microscopic studies were complemented by cathodoluminescence (CL) investigations on carbon-coated, polished thin sections using an HC1-LM optical CL microscope (LUMIC, Bochum, Germany) [40]. Analytical conditions were set at 14 kV accelerating voltage and a current of 0.2 mA. Luminescence images were recorded by a Peltier cooled digital video-camera (OLYMPUS DP72, OLYMPUS Deutschland GmbH, Hamburg, Germany) and CL spectra measured with an Acton Research SP-2356 digital triple-grating spectrograph coupled to a Princeton Spec-10 CCD detector (OLYMPUS Deutschland GmbH, Hamburg, Germany) in the wavelength range 380 to 1000 nm. The measurements were performed under standardized conditions (wavelength calibration with an Hg-halogen lamp, spot width 30 µm, measuring time 1 s).

Mineral identification was performed using a combination of structural (X-ray diffraction, XRD) and chemical information (scanning electron microscopy energy dispersive X-ray analysis, SEM-EDX). SEM measurements (secondary electrons—SE, back-scattered electrons—BSE) including local chemical analyses (EDX) were performed on carbon-coated thin sections and sample pieces using a JEOL JSM-7001F (20 kV, 2.64 nA, JEOL Ltd., Akishima, Japan) with a BRUKER EDX system (Quantax 800). In addition, sample pieces without carbon-coating were analyzed using a ZEISS EVO 10 SEM (Carl Zeiss, Oberkochen, Germany) coupled with a BRUKER Quantax EDS system (XFlash 410-M).

The mineralogical composition of separated and prepared (<20 µm) fractions was analyzed by X-ray diffraction using a URD 6 Bragg–Brentano diffractometer (Seifert/Freiberger Präzisionsmechanik, Freiberg, Germany) with Co-K $\alpha$  radiation and a METEOR 0D Si drift detector (GE Sensing & Inspection Technologies GmbH, Ahrensburg, Germany) in the range of 5–80° (2 $\theta$ ). Analytical conditions

included a detector slit of 0.25 mm, 0.03° step width, and 5 s measuring time. Due to the limited amount of sample material, smear mounts of the material suspended in ethanol were prepared on Si low-background holders. Data were evaluated qualitatively using the ANALYZE RayfleX v.2.352 software. The SEARCH-MATCH procedure for non-clay minerals was based on automated routines and user-guided evaluation of their results, employing the ICDD PDF4+ database (2019 issue). For the identification of smectite minerals, additional measurements with oriented slides of untreated and ethylene glycol saturated samples were performed to analyze the swelling behavior.

Filament morphometries were described by imaging filaments and filament-like structures in polished thick (150 µm) sections using a Leica DM4500P microscope (Leica Microsystems, Wetzlar, Germany). Images of microbial filaments and of fibrous/filamentous inorganic precipitates and minerals were obtained from slide mounts prepared with water or immersion oil. For extended depth of field, images were taken using the Leica Application Suite software (LAS 4.5.0) including extended depth of field. Both filament diameters and filament shapes were measured on the obtained images using the ImageJ software (version 1.51m9). For filament shape determinations, filaments were digitized as point tracks using the “Multi point” tool of ImageJ. Point tracks for single filaments were further analyzed in Excel for the determination of (i) total length, (ii) distance between first and last point, (iii) tortuosity (i/ii), (iv) bending (sum of angles between all joining segments defined by two points each) and (v) direction changes, i.e., all situations where the sense of bending changes. The morphological characteristics of MDP filamentous fabrics were compared with those of broadly similar aggregates of filamentous/fibrous/thread-like forms of minerals, glasses, and “chemical garden” precipitates of certain non-biological origin, as well as with broadly similar shapes and textures of certain biological origin. The method applied here was used first by Hofmann et al. [8] and in a slightly adapted form by Williams et al. [41].

For the detection of organic residues in selected SFF, desilicification of the central filamentous core was carried out at room temperature using a 10% hydrofluoric acid (HF) treatment over four days. The insoluble residue was carefully separated from the solution and washed with deionized water over 2 h until a neutral pH was reached.

The staining process began with immersion of the selected specimen in 20 µL of a solution containing 10 g glycerin and 10 g NaOH in 90 mL water. After 30 s, Calcofluor White (CFW) solution, a highly-sensitive blue fluorescent dye for the identification of polysaccharides containing β-glycosidic bonds such as chitin and cellulose in fossil samples [42,43] was added to the pretreated specimen for 12 h without light at room temperature. Afterwards, the sample was repeatedly washed with distilled water to eliminate the unattached CFW and dried in air at ambient temperature. Optical and fluorescence microscopy imaging on the obtained residues was performed using a BZ-9000 (Keyence, Osaka, Japan) microscope.

In addition, attenuated total reflectance Fourier transform infrared spectroscopy (ATR-FTIR) was used for the qualitative characterization of the isolated materials. The samples were analyzed using a Nicolet 210c spectrometer (Thermo Scientific, Waltham, MA, USA). These analyses were complemented by electrospray ionization mass spectrometry (ESI-MS). For that purpose, the demineralized matter was hydrolyzed in 6M HCl for 24 h at 90 °C. Next, the obtained solution was filtrated with a 0.4 µm filter and freeze-dried to remove the excess HCl. The solid remainder was dissolved in water for ESI-MS analysis. Standard d-glucosamine as a control was purchased from Sigma (Darmstadt, Germany). All ESI-MS measurements were performed on an Agilent Technologies 6230 TOF LC/MS spectrometer (Applied Biosystems, Foster City, CA, USA). Nitrogen was used as a nebulizing and desolvation gas. Graphs were generated using Origin 8.5.

## 4. Results

### 4.1. Morphology of SFF

The SFF occur in the open space of cavities and exhibit a wide variation in macroscopic morphology (Figure 5) and size (up to 10 cm, in extreme cases up to 100 cm in the Jamner area). At least eight different types of filament morphologies observed (Figure 5) can be grouped into two basic categories. Types 1–7 consist of parallel straight or curved linear filaments or filament intergrowths (Figure 2a,b). Type 8 can be characterized as planar matted fabrics (Figure 2c).

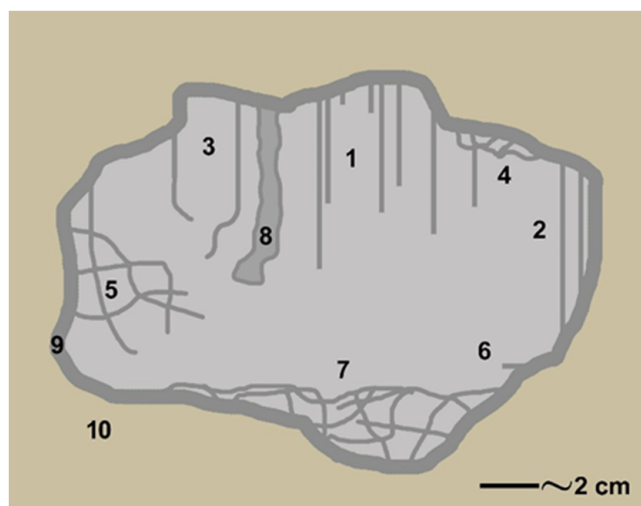


**Figure 5.** Schematic sketch of a cavity showing different morphological varieties of SFF: (1) Gravity-controlled linear SFF (pseudo-stalactite). (2) Coalescence of type 1 SFF with the cavity walls. (3) Gravity-controlled SFF growth continuing unoriented. (4) SFF randomly intergrown with the cavity margin. (5) Formation of stable frames of randomly oriented and curved SFF. (6) SFF with horizontal orientation and maximum length of 3 cm. (7) Cavity bottom with masses of irregular SFF embedded in chalcedony. (8) SFF consisting of intergrown filaments forming planar matted fabrics. (9) Wall lining consisting of clay minerals and chalcedony layer. (10) Dense unaltered host rock of the lava core zone. Note that individual SFF showing upward growth (“pseudo-stalagmites”) were not detected.

The most common is type 4, forming a thin layer up to 1 cm thick at the cavity ceiling/walls, as well as type 7, forming layers up to a few centimeters thick at the cavity bottom. The gravity-controlled types 1–3 commonly consist of several single, parallel grown filaments, which are joined together by chalcedony resulting in shapes resembling stalactites. Type 5 SFF are not very common but can develop intergrowths up to 15 cm in height. In the following, SFF types 1–7 are labeled as SFF<sub>Ir</sub> (irregular) and matted type 8 as SFF<sub>Ma</sub> (matted).

The cross-sections of SFF<sub>Ir</sub> are characterized by round or irregular shapes resulting from the intergrowth of several SFF<sub>Ir</sub> (Figure 6a–e). In contrast, the cross-sections of SFF<sub>Ma</sub> are developed as band-like forms (Figure 6f).

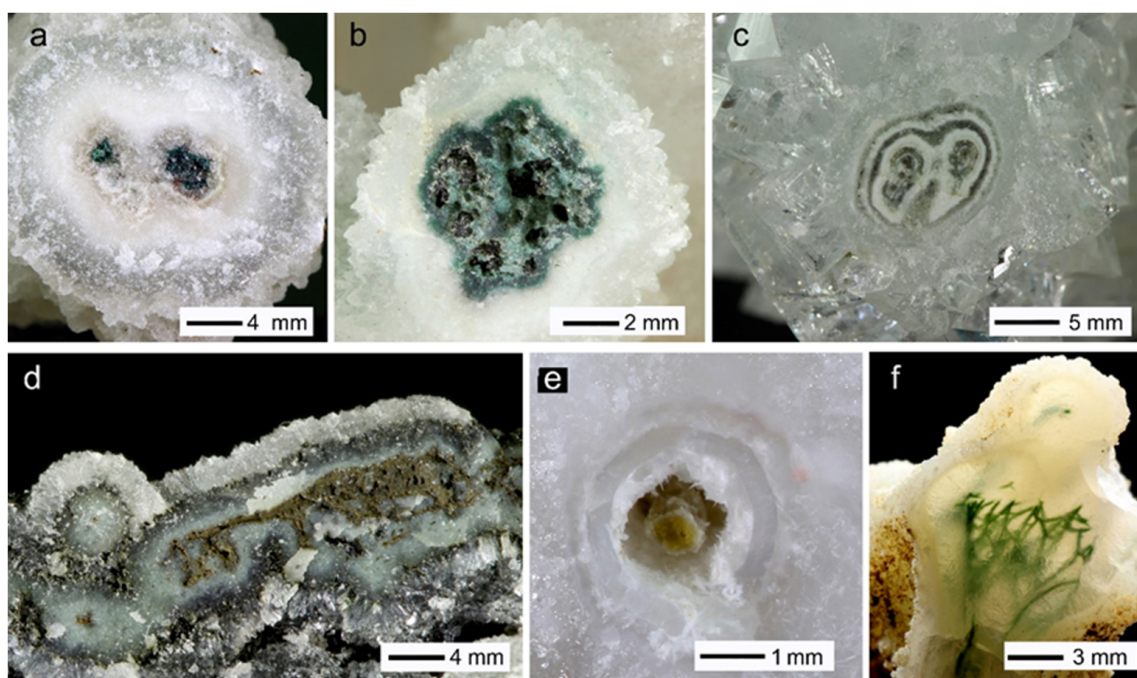


**Figure 6.** Cross-sections of SFF representing different structures: (a) Two separate core zones overgrown by silica, amalgamated to one SFF<sub>Ir</sub>. (b) Several directly connected core zones, overgrown by silica. (c) Two separate core zones surrounded by clay minerals and alternating silica layers. (d) Several separate and connected core zones overgrown by silica and enclosed clay minerals. (e) One core zone surrounded by an empty space, zeolite, and finally silica. (f) Several core zones overgrown by silica forming a tabular matted sheet SFF<sub>Ma</sub>.

#### 4.2. Mineralogical Composition and Micro-Texture of SFF

While the macro-morphology of the different filament types is relatively easy to recognize and characterize, the mineralogical composition and micro-texture of the filaments are very complex and require a detailed and integrated study. Therefore, several SFF from different locations and of different types were selected to determine the general mechanisms of formation.

##### 4.2.1. Jalgaon/Savda

Four different samples from cavities within the quarry complex of Jalgaon/Savda were selected to clarify two aspects of the filament mineralization. First, the comparison of the mineralization sequence from the cavity walls shows the same succession as for the filament mineralization. Therefore, a profile from the host rock to the silica mineralization was studied. Second, cross-sections of filament aggregates were prepared to determine the mineralization sequence and to provide information about the characteristics of the silica minerals.

Samples Jal 30 and Jal 31 represent a mineralization profile at the cavity wall from the host rock through the mineralization sequence as well as a cross-section of a filament from the same mineralization site (Figure 7a,b). The profile shows five clearly distinguishable zones (compare Figure 7a).

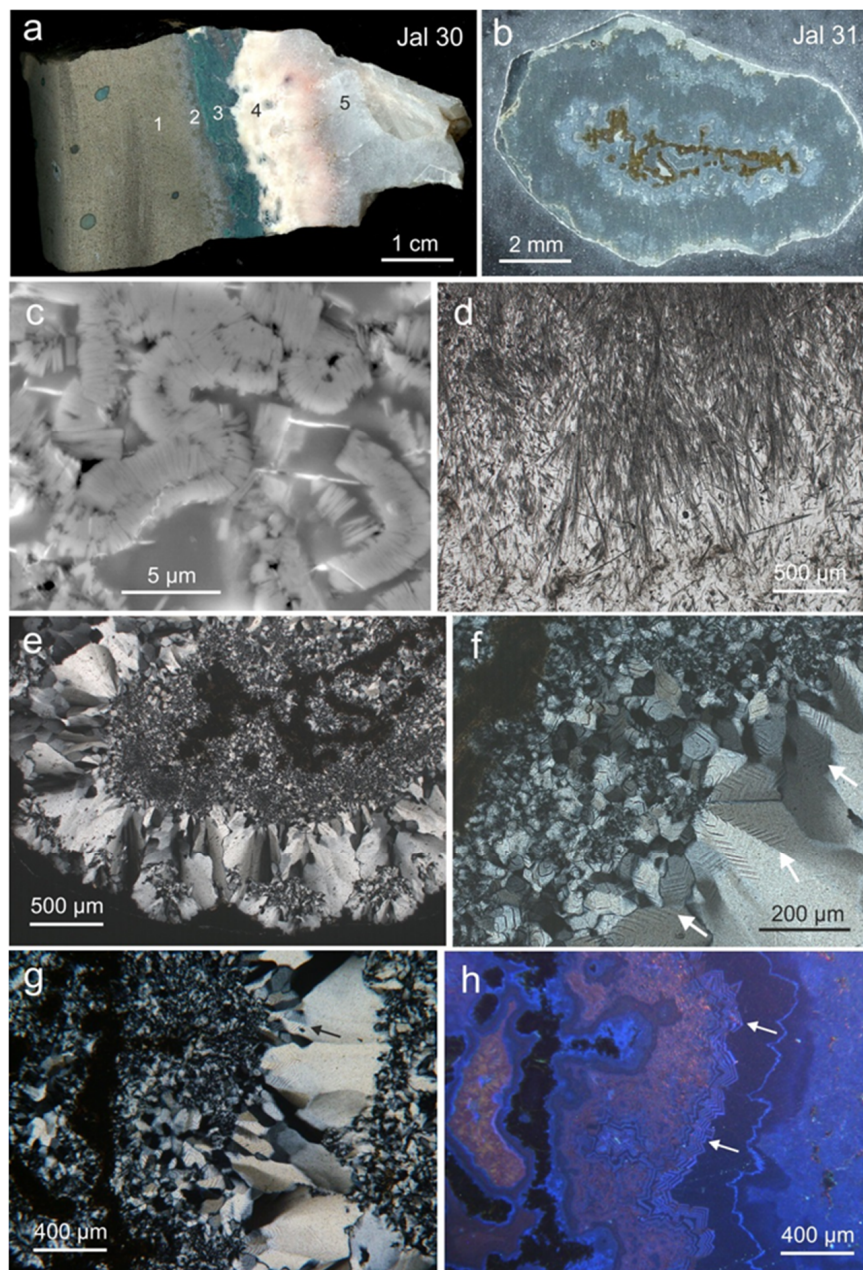


**Figure 7.** Images and micrographs showing the characteristic composition and texture of samples Jal 30 and Jal 31 (Jalgaon/Savda): (a) hand specimen showing the typical transition zone between basaltic host rock and mineralization from a cavity of the outcrops in Jalgaon/Savda (sample Jal 30), with numbers relating to different zones (for explanation see text); (b) cross-section of a filament from a cavity in Jalgaon/Savda (sample Jal 31) showing an irregular brown core filament; (c) SEM micrograph of zone 3 showing agglutinated platelets of celadonite forming worm-like textures; (d) transmitted light micrograph of acicular mordenite bundles within a homogeneous  $\text{SiO}_2$  matrix; (e) transmitted light (crossed polars) micrograph showing the filament center encrusted with micro- and macro-crystalline quartz; (f) details of the filament cross-section illustrating the  $\text{SiO}_2$  mineralization directly on the core filament surface and the succeeding grain-coarsening during crystallization, note the  $\mu\text{m}$ -sized growth lamellae (arrows), so-called Bambauer quartz; (g,h) polarized light/cathodoluminescence (CL) micrograph pair revealing the zoned crystallization sequence of silica phases, the zones with growth lamellae being clearly visible in CL (see arrows).

The host rock (zone 1) is composed of tholeiitic basalt. Data from the literature show a variable chemical composition of the tholeiitic basalt from the investigated outcrops with 49.93–51.96 wt. %  $\text{SiO}_2$ , 13.28–14.76 wt. %  $\text{Al}_2\text{O}_3$ , 12.73–14.00 wt. %  $\text{Fe}_2\text{O}_3$  ( $\text{Fe}^{2+}$  and  $\text{Fe}^{3+}$  given as  $\text{Fe}_2\text{O}_3$ ), 9.19–10.55 wt. %  $\text{CaO}$ , 4.43–6.85 wt. %  $\text{MgO}$ , 2.35–2.95 wt. %  $\text{Na}_2\text{O}$ , 0.48–0.54 wt. %  $\text{K}_2\text{O}$ , and 1.86–3.13 wt. %  $\text{TiO}_2$  [36,44]. The basalt is variably fresh and has a fine-grained, intersertal texture with some cm-sized plagioclase phenocrysts (labradorite  $\text{An}_{60}$ ) and altered olivine. In the fine-grained groundmass, fresh lath-shaped plagioclase microliths and clinopyroxene (augite) are preserved, whereas former glass and olivine are absent or replaced by brown, greenish-brown or green sheet silicates and opaque ore minerals (ilmenite-rutile-leucosene and hematite). In the transition to zone 2, di- and trioctahedral clay minerals (smectite) increasingly occur reflecting the progressive alteration process.

The green layer (zone 3 in Figure 7a) is dominated by celadonite  $\text{K}(\text{Mg}, \text{Fe}^{2+})(\text{Fe}^{3+}, \text{Al})[(\text{OH})_2/\text{Si}_4\text{O}_{10}]$  partly intergrown with stilbite and quartz (Figure 8). The celadonite is visible as agglutinated platelets forming worm-like textures (Figure 7c). The chemical composition determined by local analysis with SEM-EDX is presented in Table S1.

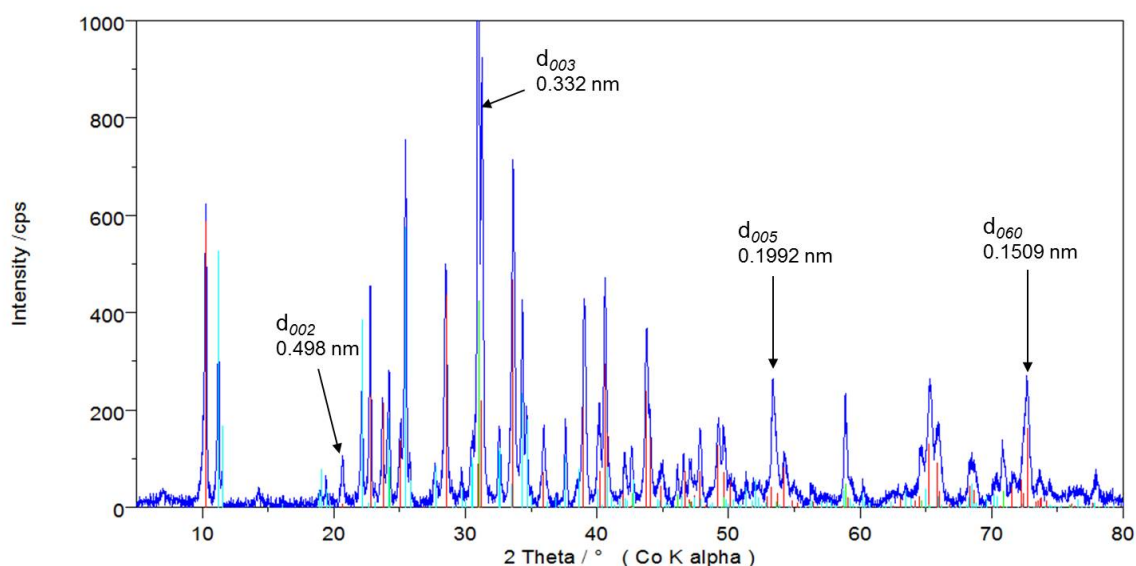


**Figure 8.** X-ray diffraction pattern of sample Jal 30 (smear powder on Si low background holder, background corrected); intensity ratios are biased by preferred orientation, beam overflow, and insufficient particle statistics; search-match results in stick patterns: red: celadonite 1M (see arrows, PDF 04-011-7885), light blue: stilbite (Ca) (PDF 01-079-1676), green: quartz (PDF 01-075-8322); the  $d_{060}$  spacing of 0.1509 nm typically indicates a dioctahedral but iron-rich mica phase.

Zone 4 starts with bundles of acicular crystals of zeolites intergrown in a matrix of micro-crystalline silica (Figure 7d). XRD analyses, polarizing microscopy, and spatially resolved chemical analyses (Table S1) show that the zeolite is predominantly mordenite ( $(\text{Ca}, \text{K}_2, \text{Na}_2)[\text{AlSi}_5\text{O}_{12}]_2 \cdot 7\text{H}_2\text{O}$ ) which crystallizes together with micro-crystalline chalcedony and macrocrystalline quartz. The precipitation of  $\text{SiO}_2$  continued and formed zone 5, which consists almost completely of pure chalcedony/quartz.

Investigations of the cross-sections of a filament of sample Jal 31 provided more details about the texture of the crystallization sequence, in particular the  $\text{SiO}_2$  phases. Figure 7e shows an overview of the filament cross-section. An irregularly branched brownish filamentous core is situated in the center of the ellipsoidal filament (Figure 7b). The chemical composition of this very fine-grained material (Table S1) shows high contents of Si, Fe, Mg, and Al as well as remarkable concentrations of Ca, K, and Na. As a result of the lack of XRD analyses, due to the limited sample material, it can only be speculated from the chemistry that clay minerals (smectite) and probably celadonite are possible

mineral constituents. On the other hand, amorphous compounds and iron oxides/-hydroxides can also be assumed to be present in this initial state.

The precipitation of silica phases starts directly at the surface of the brown filamentous core. The filamentous core is encrusted by multiple layers of SiO<sub>2</sub> that show coarsening of grain size from central micro-crystalline chalcedony to macro-crystalline quartz at the margin (Figure 7e,f). XRD analyses of early silica precipitates also show the presence of opal-CT and cristobalite indicating a formation via an amorphous silica precursor (Figure 9). The coarse quartz crystals exhibit characteristic μm-sized growth lamellae (see arrows in Figure 7f), so-called Bambauer quartz. The occurrence of different SiO<sub>2</sub> generations is confirmed by CL investigations (Figure 7g,h). Varying CL colors point to different crystallization steps. Even homogeneously appearing crystals show heterogeneous internal textures. The growth lamellae are highlighted in CL (arrow in Figure 7h).

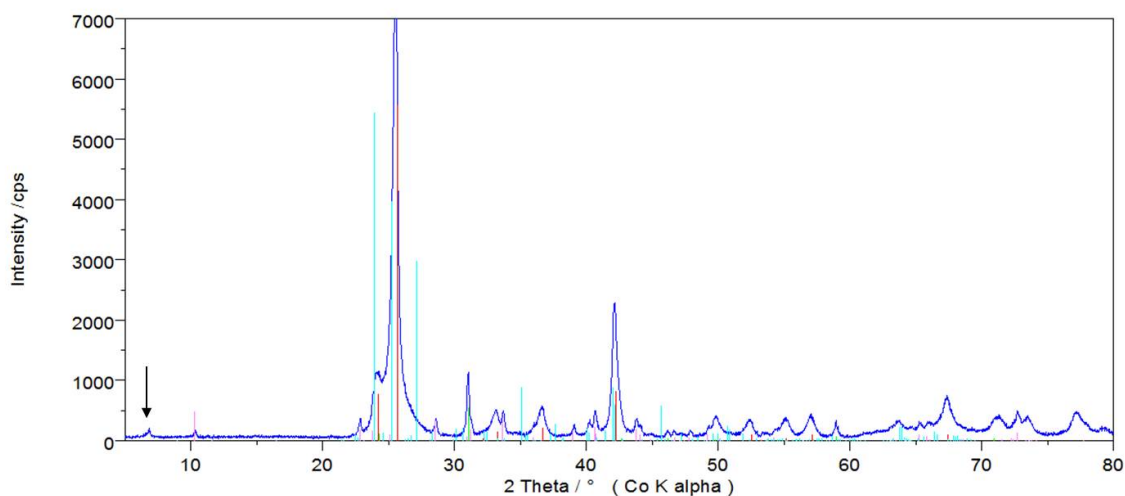


**Figure 9.** X-ray diffraction pattern of sample Jal 31 (powder sample, background corrected); search-match results in stick patterns: red: opal-CT (PDF 00-066-0177), light blue: tridymite (PDF 04-008-8127) as a proxy for more “tridymitic” opal-CT, for comparison only, green: quartz (PDF 01-075-8322); the arrow points to the  $d_{001}$  of smectite with 1.498 nm.

Samples Jal 32 and Jal 33 provide further information about the microstructure of the filaments from the quarry area of Jalgaon/Savda (Figure 10). Sample Jal 33 represents a cross-section of two conical filaments with dark brown cores (Figure 10a). The core is encrusted by a concentric succession of silica layers with varying grain size (Figure 10c) and textural characteristics indicating changes in the physicochemical conditions during crystallization. The outermost filament layer of several 100-μm thickness is composed of macro-crystalline quartz. The short-lived bluish CL (Figure 10e,f) is characteristic for quartz crystallized from aqueous solution at elevated temperatures. Details of the filamentous core (Figure 10d) reveal an Fe-rich composition (high BSE contrast) and an irregular texture with dissolution features. The chemical composition is similar to that of the core of sample Jal 30 dominated by Si, Fe, Mg, and Al (see Table S1).

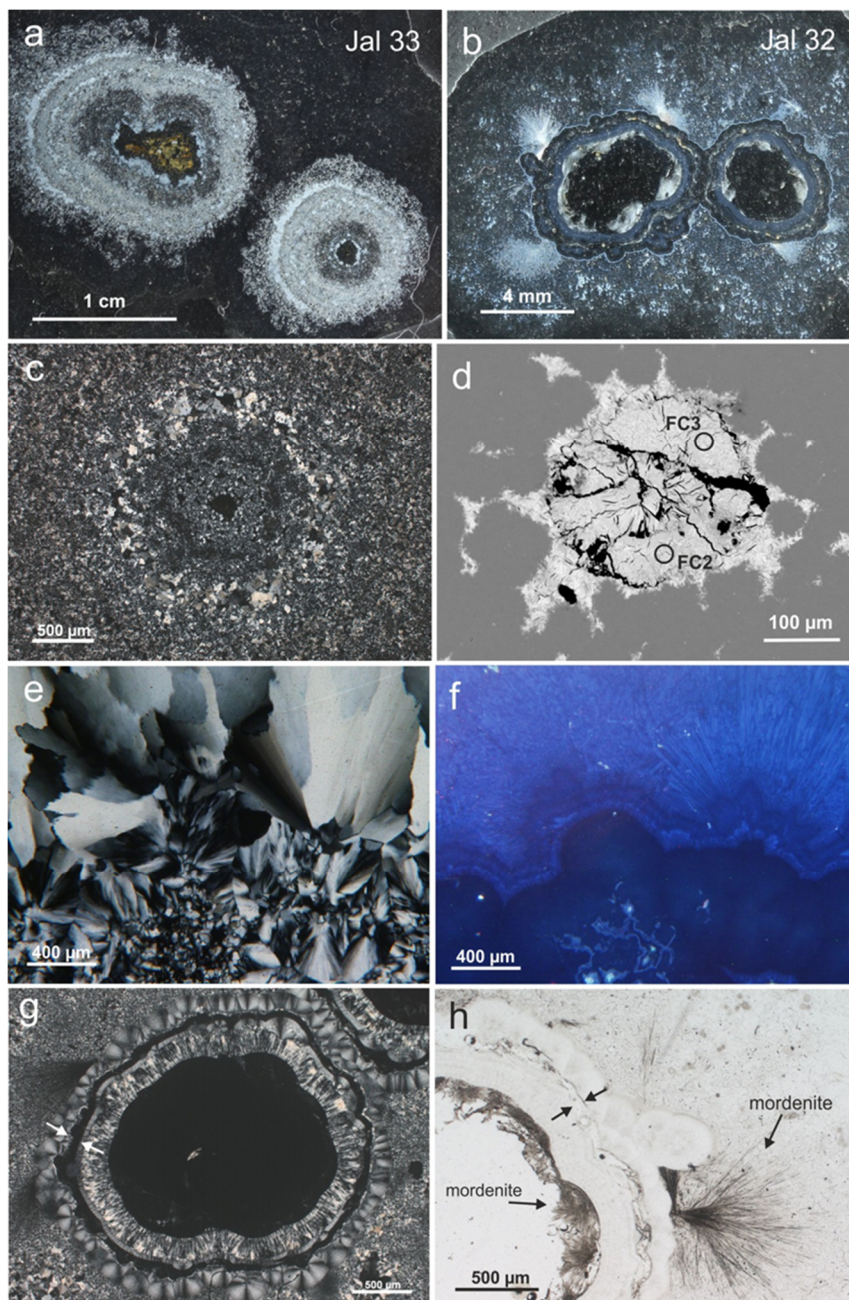


**Figure 10.** Microstructural features of two filamentous cores from Jalgaon/Savda, India: (a) cross-section of two conical SFF with filamentous cores showing a dark-brownish filament center (sample Jal 33); (b) cross-section of SFF with two empty filamentous cores (sample Jal 32); (c) micrograph in transmitted light (crossed polars) of the central part of the right filamentous core in Figure 10a; the dark core is encrusted by concentric layers of chalcedony showing varying grain size; (d) SEM-BSE image of the filamentous core in sample Jal 33 (compare (c)) with bright contrast due to high Fe contents and irregular dark fissures; FC2 and FC3 mark the analytical points of EDX measurements (see data in Table S1); (e,f) transmitted light (crossed polars) (e) and CL (f) images showing textural details of the SiO<sub>2</sub> mineralization sequence; (g) micrograph in transmitted light (crossed polars) of the central part of the filamentous core in (b) (sample Jal 32), the core being empty and surrounded by concentric layers of fine-grained and fibrous SiO<sub>2</sub>; the arrows point to an empty concentric layer within the silica succession; (h) close-up of the central part of sample Jal 32; mordenite crystallized inwards to the central hole and within the silica matrix; note the empty space (arrows) between the silica layers.

The cross-section of sample Jal 32 (Figure 10b) shows an SFF with filamentous core zones made up of a central hole (ca. 3 mm in diameter) encrusted by concentric layers of silica phases with different grain size and texture (granular and fibrous; Figure 10g). These variations can probably be ascribed to variations in the growth conditions during silica precipitation. The texture of the innermost fibrous chalcedony layer indicates that it grew on a former matrix, which dissolved afterwards. Indications for dissolution processes of former existing material are also given by the empty tubular interspace within the silica succession (see arrows in Figure 10g,h). Bundles of acicular crystals grew both into the central hole as well as within the silica matrix (Figure 10h). XRD and local chemical analyses (see Table S1) revealed that the crystals are mordenite, the zeolite with the highest SiO<sub>2</sub> content.

Sample Jal 11 represents a chalcedony aggregate with two central filamentous cores (Figure 11a). The cross-section of the aggregate (Figure 11b,c) reveals that the unattached, freely movable filamentous core is surrounded by a tubular space with circular profile followed by further mineralization of white, fibrous crystals and SiO<sub>2</sub> mineralization. The disconnection of the core filament from the main sample allowed for detailed investigation of this central structure. The SEM micrographs in Figure 11d–f show the external shape of the separated core filaments as well as details of the surface and a longitudinal cut with the inner structure of the filament.

The SEM micrograph in Figure 11d shows the surface morphology of the core filament, which is characterized by numerous constrictions indicating shrinkage cracks. At high magnification, details of the surface structure are visible with agglutinated platelets forming irregular frameworks (Figure 11e). Such textures are typical of several clay minerals, in particular minerals of the smectite group. XRD measurements produced a  $d_{060}$  reflex at 1.50 Å, confirming the presence of a dioctahedral smectite mineral (Figure 12). The sample treatment with glycol resulted in a widening of the sheet parameters from 15 to 17 Å due to swelling. Additional local chemical analyses by SEM-EDX (Table S2) indicate that the swellable dioctahedral smectite is a Fe-poor montmorillonite with an average crystal chemistry composition on a water-free basis of  $(\text{Ca}_{0.25}\text{Na}_{0.10})\text{Si}_4(\text{Al}_{1.25}\text{Fe}^{3+}_{0.15}\text{Mg}_{0.60})[\text{O}_{10}(\text{OH})_2]$ .

Another characteristic feature of the filament surface is the occurrence of fibrous minerals (Figure 11e). The morphology and chemical composition of these mineral fibers (compare Table S2) indicate a mineral of the zeolite group, most likely mordenite  $((\text{Ca}, \text{Na}_2, \text{K}_2)[\text{AlSi}_5\text{O}_{12}]_2 \cdot 7\text{H}_2\text{O})$ . XRD measurements confirm the presence of mordenite. The cations Ca, Na, and K are exchangeable resulting in slightly varying chemical compositions. Mordenite in the investigated samples is dominated by Ca and essentially free of K.

The same results were obtained for the fibrous mineral aggregates which occur at the inner surface of the tubular space (Figure 11b,c). Both SEM-EDX analyses and XRD measurements confirmed the presence of mordenite. Needle-like crystals of mordenite are also intergrown with the first generation of SiO<sub>2</sub>, before further mineralization sequence results in more or less pure silica minerals.

The careful preparation of the core filament by a longitudinal cut revealed insights into the inner structure (Figure 11f). The whole filament with a diameter of 0.2–0.5 mm consists of several filament strands with diameters of approx. 50 µm each. The innermost part of these strands is composed of linear threads of approx. 20 µm in diameter, whereas the outer region is characterized by a honeycomb arrangement resembling a cell structure (Figure 11f).

Sample Jal 05 is a large SFF-type chalcedony aggregate with multiple greenish, zoned filament core aggregates from Jalgaon/Savda (Figure 13a). The cross-section of the filamentous aggregates reveals different concentric mineralization layers with fine-grained greenish-brown minerals in the central part (Figure 13b).

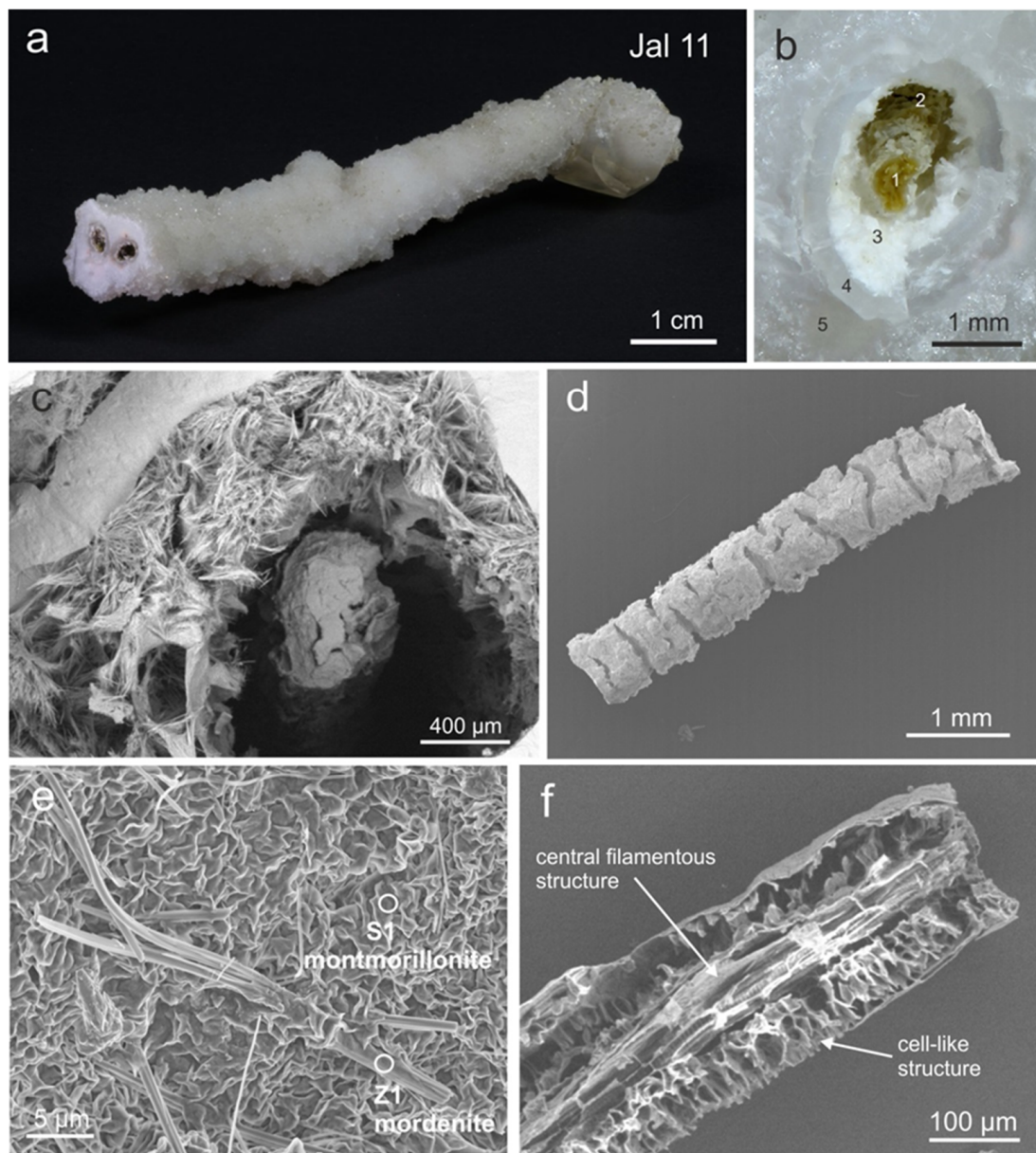


**Figure 11.** Micrographs of sample Jal 11 (Jalgaon/Savda). (a)  $\text{SiO}_2$  aggregate showing two filamentous cores. (b) Cross-cut of the  $\text{SiO}_2$  aggregate showing a greenish filamentous core (1), a tubular hole around the filament core (2), needle-like crystals of zeolites (mordenite (3)), chalcedony intergrown with mordenite (4) and more or less pure chalcedony (5). (c) SEM micrograph showing details of the cross-section with filamentous core and surrounding hole as well as fibrous crystals of mordenite. (d) SEM image of a loose part of a filamentous core. (e) Magnified part of (d) showing an irregular surface of smectite (montmorillonite) and mordenite fibers; S1 and Z1 relate to the EDX measurements in Table S2. (f) SEM image of a longitudinal cut of a filamentous core (200  $\mu\text{m}$  diameter) showing a central fibrous structure (ca. 20–40  $\mu\text{m}$ ) and a marginal cell-like structure; the inner filament zone consists of several thread strands with a diameter of approx. 5  $\mu\text{m}$ .

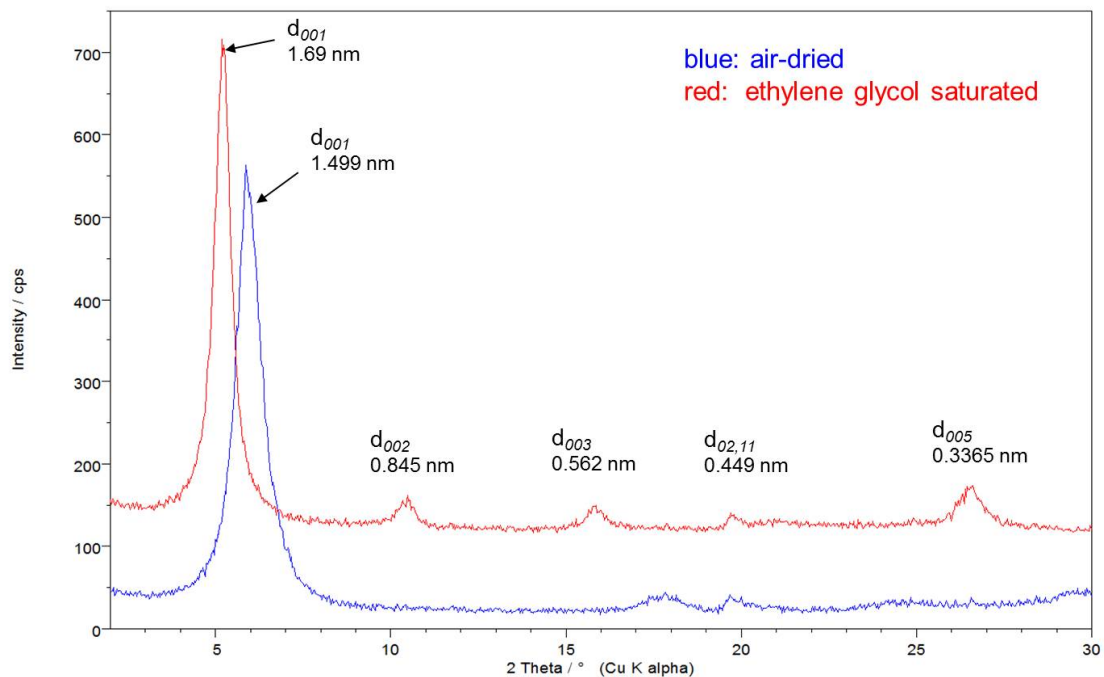


**Figure 12.** X-ray diffraction patterns of sample Jal 11 (oriented slide, air-dried and saturated by ethylene glycol, y-offset 100 cps); the pattern in ethylene glycol saturated state shows full swelling and a rational series of basal reflections of dioctahedral smectite.

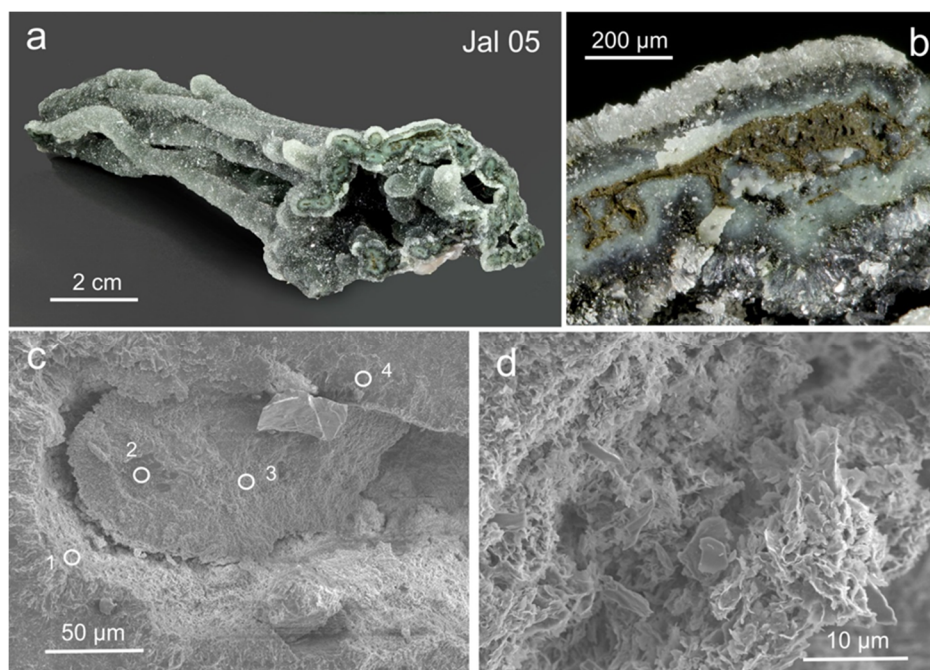


**Figure 13.** Morphological and textural features of sample Jal 05 from secondary mineralization in cavities of flood basalt of Jalgaon/Savda, India: (a) large, multi-filamentous chalcedony aggregate with greenish, zoned core; (b) details of the different concentric mineralization layers with fine-grained greenish-brown minerals in the central filamentous cores; (c) cross-section (SEM-SE micrograph) of the central part of an aggregate with a filamentous core and a small empty interspace to the following mineralization sequence (the numbers relate to analytical spots of EDX measurements, see Table S3); (d) close-up of (c) illustrating the fine-grained, irregular mineralization of the surface of the filamentous core.

Local chemical analyses were focused on the fine-grained filamentous core areas of the aggregates to obtain information about the nature of the initial mineralization stage. The filamentous cores may have sizes from 100 to several hundred  $\mu\text{m}$  in cross-section, sometimes with an empty space to the following mineralization sequence (mostly silica minerals; Figure 13c). At high magnification, the surface of the filament core material shows predominantly fine-grained and irregular mineralization (Figure 13d). Local chemical analyses of the core material (compare Figure 13c) show a dominance of Si, Fe, Al, Mg, and Ca. The results of Table S3 indicate that the presence of Fe-rich smectite (e.g., saponite) and/or Fe compounds is most likely. Due to the detected carbon excess, small amounts of carbonate or organic carbon could also be present. On the other hand, the lack of K indicates missing mineral phases of the mica group (e.g., celadonite) that were detected in other samples of filamentous cores.

Sample Jal Sm 01 represents a peculiarity, since the SFF lack a chalcedony/quartz overgrowth (Figure 14a). Therefore, the inner filament cores are clearly visible. The cross-section reveals a concentric structure consisting of several layers with varying colors (Figure 14b). The filamentous core is situated in the central part of the aggregate surrounded by a tubular space and followed by several mineralization layers (Figure 14c,d). The filamentous core itself shows several intergrown threads with a diameter of ca. 20  $\mu\text{m}$  and a cross-section with a spherulitic structure (Figure 14d). The lateral view of the filamentous core shows an elongated and irregular shape (Figure 14e) with a striking outer surface (Figure 14f).

Local chemical analyses of this central part reveal a varying chemical composition dominated by Si, Al, Ca, Mg, and Fe (Table S4). Moreover, the SEM-EDX analyses of carbon-coated samples showed remarkable carbon excess. To quantify the carbon content of the core filament, uncoated sample pieces were investigated by an environmental scanning electron microscope (ESEM). The results showed up to 39 at% carbon. Therefore, the determination of the mineral composition is very complicated. Assuming that at least some of the mineral phases could be non-crystalline, the chemical composition points to a mixture of clay minerals (smectite), silica phases, iron oxide/-hydroxides, and probably carbonates (calcite). However, the presence of organic carbon and/or hydro-carbon compounds cannot be excluded.

For a precise determination of the mineral phases in the green outer and interlayers of the filaments, powder XRD analyses of carefully separated material were performed. The X-ray pattern in Figure 15 shows an almost perfect 00l-series of trioctahedral smectite. The base reflex is located at 14.9  $\text{\AA}$  and the  $d_{060}$  reflex at 1.538  $\text{\AA}$ . A shift of the base reflex to 17  $\text{\AA}$  after treatment with ethylene-glycol confirmed the swelling of the sheet spacing. Considering the high Mg and Fe contents (Table S4) the data most likely point to Fe-rich saponite with an average water-free composition of approximately  $\text{Ca}_{0.30}(\text{Al}_{0.60}\text{Si}_{3.40})(\text{MgFe}_2)[\text{O}_{10}(\text{OH})_2]$ . However, a mixture of smectite with iron oxides/-hydroxides also must be taken into account. Although no crystalline iron compounds were detected by XRD, the presence of strongly disordered or amorphous iron compounds is possible.

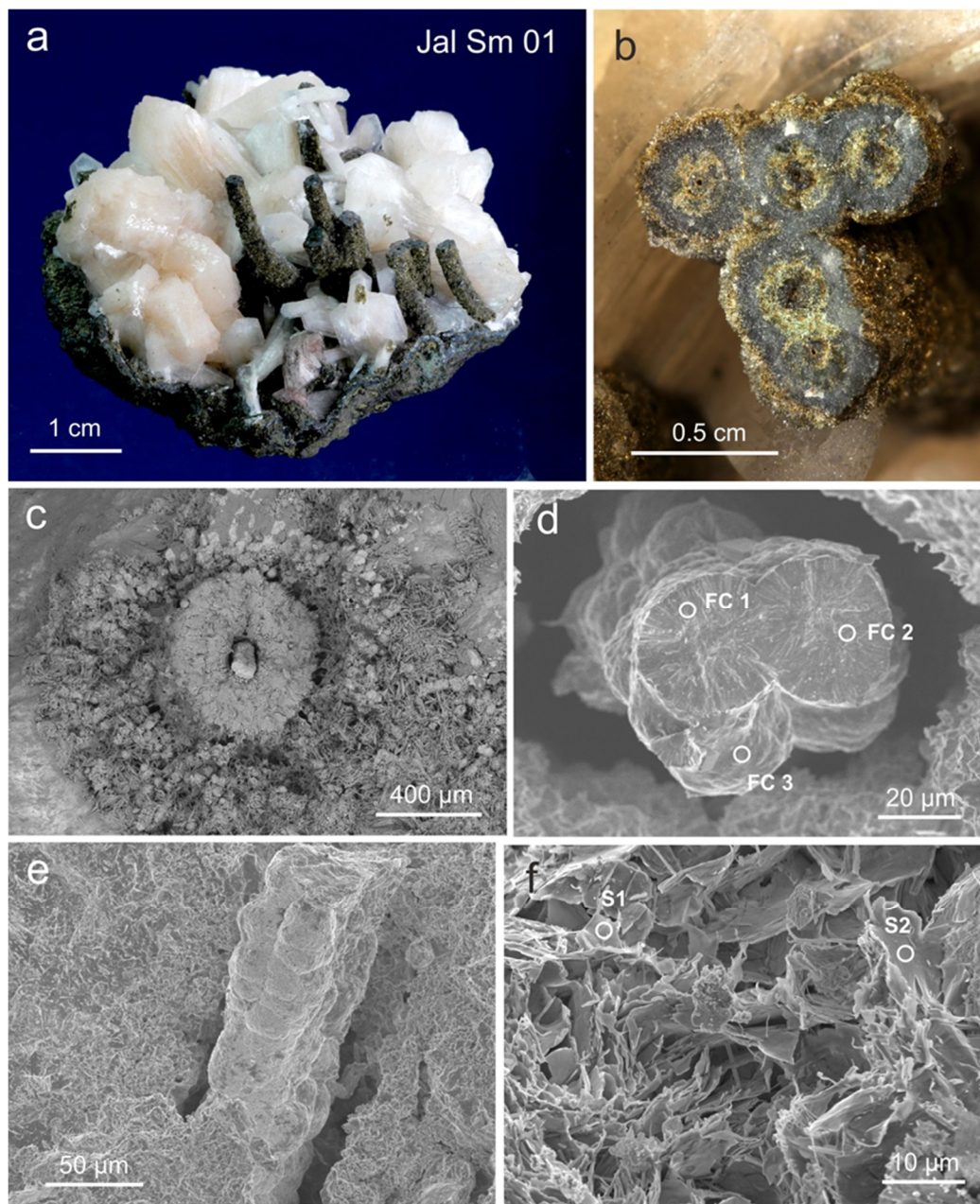


**Figure 14.** Images of sample Jal Sm 01 (Jalgaon/Savda): (a) secondary cavity mineralization showing brown filament aggregates between stilbite crystals; (b) cross-cut of the filamentous aggregates showing alternating greenish, brownish, and grey concentric layers; (c) SEM micrograph of a filamentous core with a thin innermost filament-like structure concentrically surrounded by mineral aggregates; (d) details of the innermost filamentous core of ca. 50- $\mu\text{m}$  thickness consisting of radial fibers (the numbers relate to local chemical analyses, see Table S4); note the empty space between the filamentous core and the following mineralization sequence; (e) SEM micrograph showing a lateral view of the filamentous core; (f) close-up of the surface of the filamentous core showing a frame of flaky crystals of smectite (saponite; compare chemical composition in Table S4).

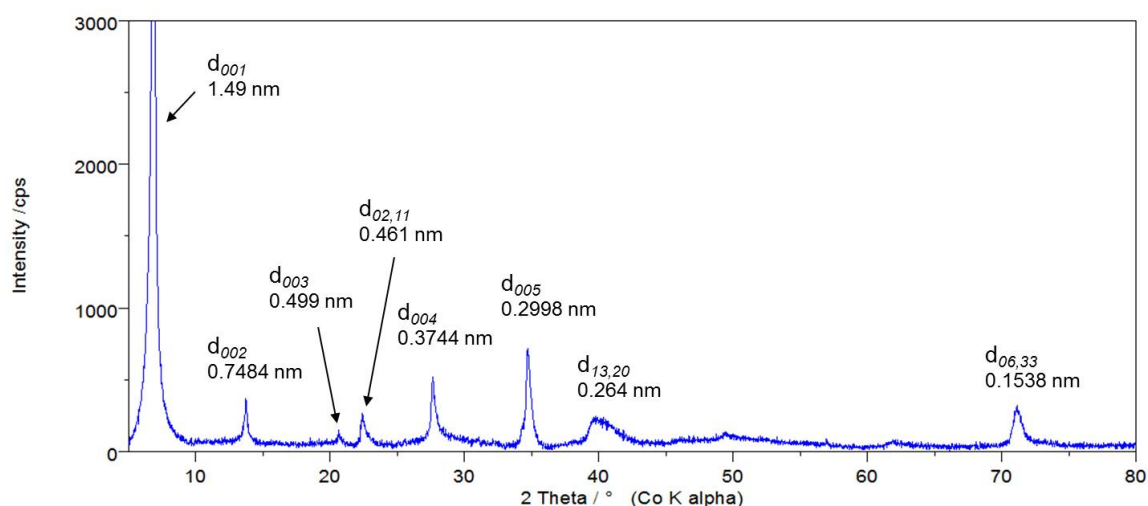


**Figure 15.** X-ray diffraction pattern of sample Jal Sm 01 (smear powder, on Si low background holder, background corrected); indexing of the smectite phase: non-basal reflections are indexed two-dimensionally according to the turbostratic disorder of the smectite phase; the  $d_{06,33}$  spacing of 0.1539 nm typically indicates a trioctahedral phase.

#### 4.2.2. Jamner

Sample Jam 01 originated from a cavity in basalts from Jamner and represents an elongated chalcedony aggregate with central filamentous cores (Figure 16a,b). The filamentous core is composed of irregular olive-green aggregates and masses in the center (Figure 16b).

Different types of filamentous shapes are visible inside the tubular central spaces. A characteristic feature is the empty space between the filamentous core(s) and the following mineralization sequence (Figure 16c), which can probably be ascribed to subsequent shrinkage processes (e.g., dehydration, degradation of organics). Separate larger structures of the core filaments are not detectable. In fact, the filamentous cores consist of vermicular, partly irregular dense masses and exhibit rough surfaces (Figure 16d).

The chemical analyses of different parts of the filamentous cores show high concentrations of Si, Fe, Al, and Mg (Table S5). XRD measurements show the presence of trioctahedral smectite (Fe-rich saponite), celadonite, and quartz. Furthermore, investigations of sample pieces without carbon-coating revealed high carbon contents up to 24 at%. Due to the relatively low Ca concentrations (compare Table S5), higher amounts of calcite can be excluded, and the existence of organic carbon must be taken into account. Non-crystalline compounds of Fe-oxides/-hydroxides and/or silica are also possible.

The following outer mineralization is dominated by  $\text{SiO}_2$  phases. XRD analyses show the predominance of quartz and an intergrowth with zeolites (mordenite) and small amounts of smectite in the first, innermost sequence of the pseudo-stalactitic aggregate.

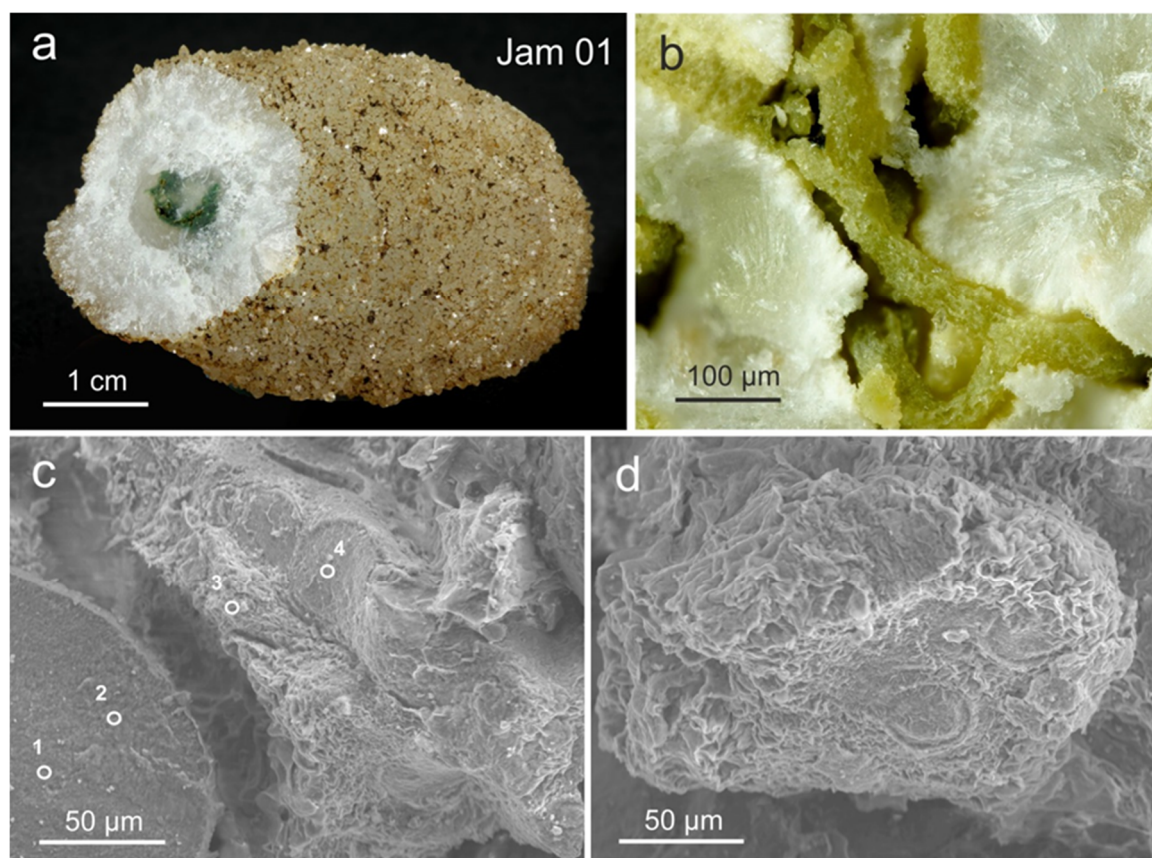


**Figure 16.** Images of sample Jam 01 (Jamner): (a) elongated SiO<sub>2</sub> aggregate inheriting an olive-green filamentous core; (b) details of the green filamentous core of the silica aggregates; (c) SEM micrograph of a dense filamentous core without recognizable texture surrounded by an empty space and the following mineralization sequence; the numbers relate to local chemical analyses by SEM-EDX (see Table S5); (d) mineralized matrix consisting of irregular masses with a rough surface texture missing visible crystals.

Sample Jam 10 derives from a cavity in the basalts of Jamner and represents an elongated chalcedony aggregate with central filamentous cores (Figure 17a,b). The filamentous core is composed of several 10 μm-sized green filamentous structures in the center (Figure 17b) and needle-like white crystals, which are radially arranged and extend into the small hollow. These fibrous crystals are intergrown with and surrounded by silica minerals. Mineralogical investigations by XRD and local chemical analyses by SEM-EDX revealed that the core material consists of dioctahedral 1M mica and different zeolites (heulandite-clinoptilolite, stilbite, mordenite; Figure 17, Table S6). The mica mineral has a base reflex at 1.51 Å and contains considerable amounts of iron, indicating that this is most likely celadonite. According to XRD results, small amounts of smectite are probably intergrown with celadonite.

Detailed investigations by SEM (Figure 17c–f) show that zeolites with heulandite-clinoptilolite composition form platy crystals (Figure 17c) and stilbite massive blocky crystals (Figure 17f), whereas mordenite preferentially exists as bundles of fibrous crystals (Figure 17d). In general, the filamentous core is extremely fine-structured. Celadonite and zeolites form networks and tubular fabrics (approx. 50 μm diameter) of fibrous crystals and needles (Figure 17e), which probably originally covered the innermost filament threads. Furthermore, different silica phases were detected in the filamentous core.

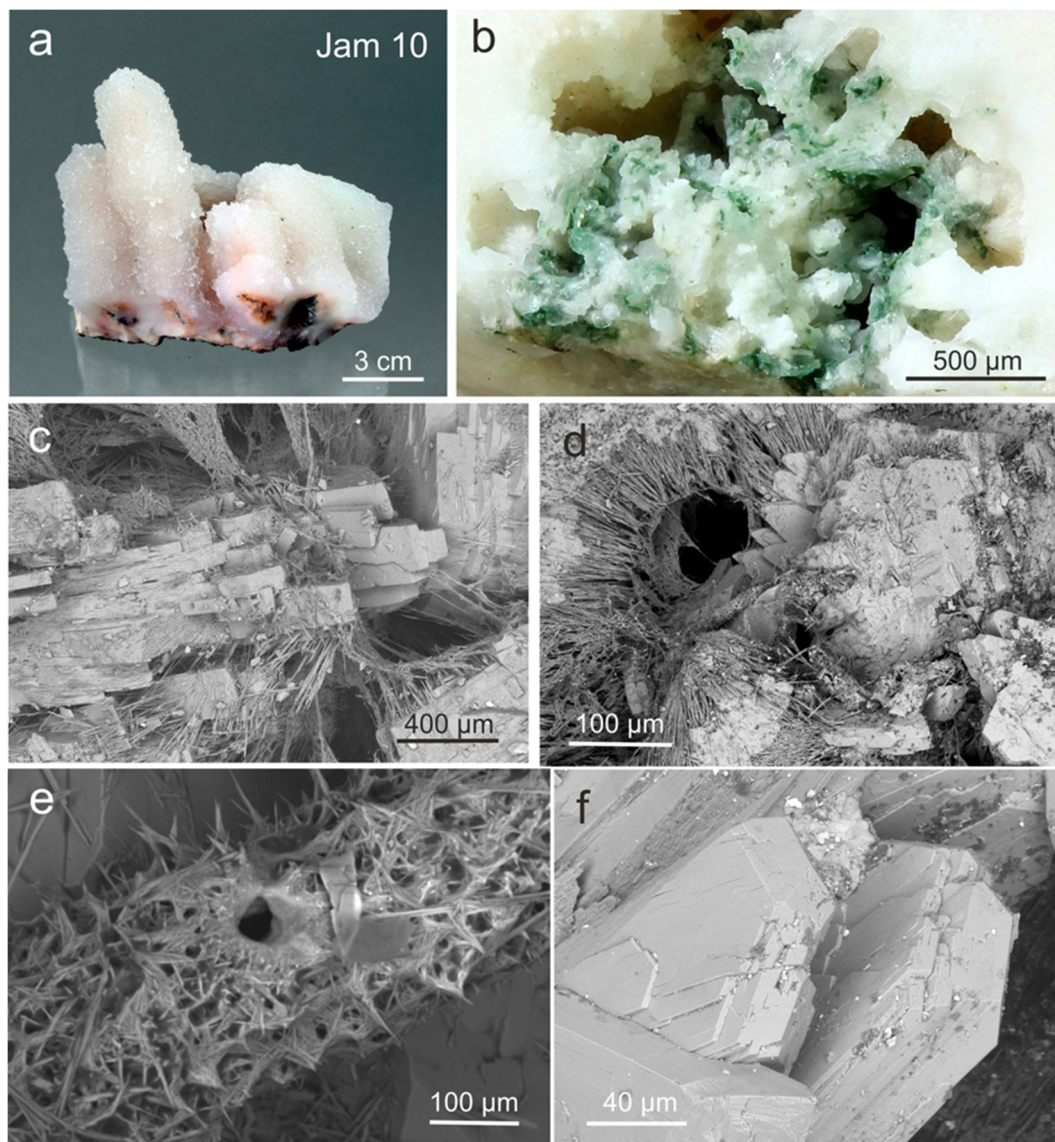


**Figure 17.** Images of sample Jam 10 (Jamner): (a) pseudo-stalactitic  $\text{SiO}_2$  aggregate inheriting filamentous cores; (b) details of the green filamentous center of the silica aggregates; (c) SEM micrograph of zeolites showing platy heulandite-clinoptilolite crystals overgrown by fibrous mordenite; (d) SEM image of a spherical hole surrounded by heulandite-clinoptilolite and fibrous bundles of mordenite; (e) tubular, reticular aggregate (probably surrounding the former filamentous core) consisting of fine filaments several  $\mu\text{m}$  in diameter (celadonite) and adhering mordenite fibers; (f) SEM micrograph of blocky stilbite crystals; for chemical analyses of the minerals see Table S6.

#### 4.2.3. Jalna

Sample Jln 01 represents a network of elongated, intergrown chalcedony aggregates (Figure 18a), which derive from an outcrop at Jalna. The fractured surface reveals numerous dark green filamentous cores (Figure 18b). The green filamentous cores are embedded in clear silica mass and surrounded by micro- and macrocrystalline quartz.

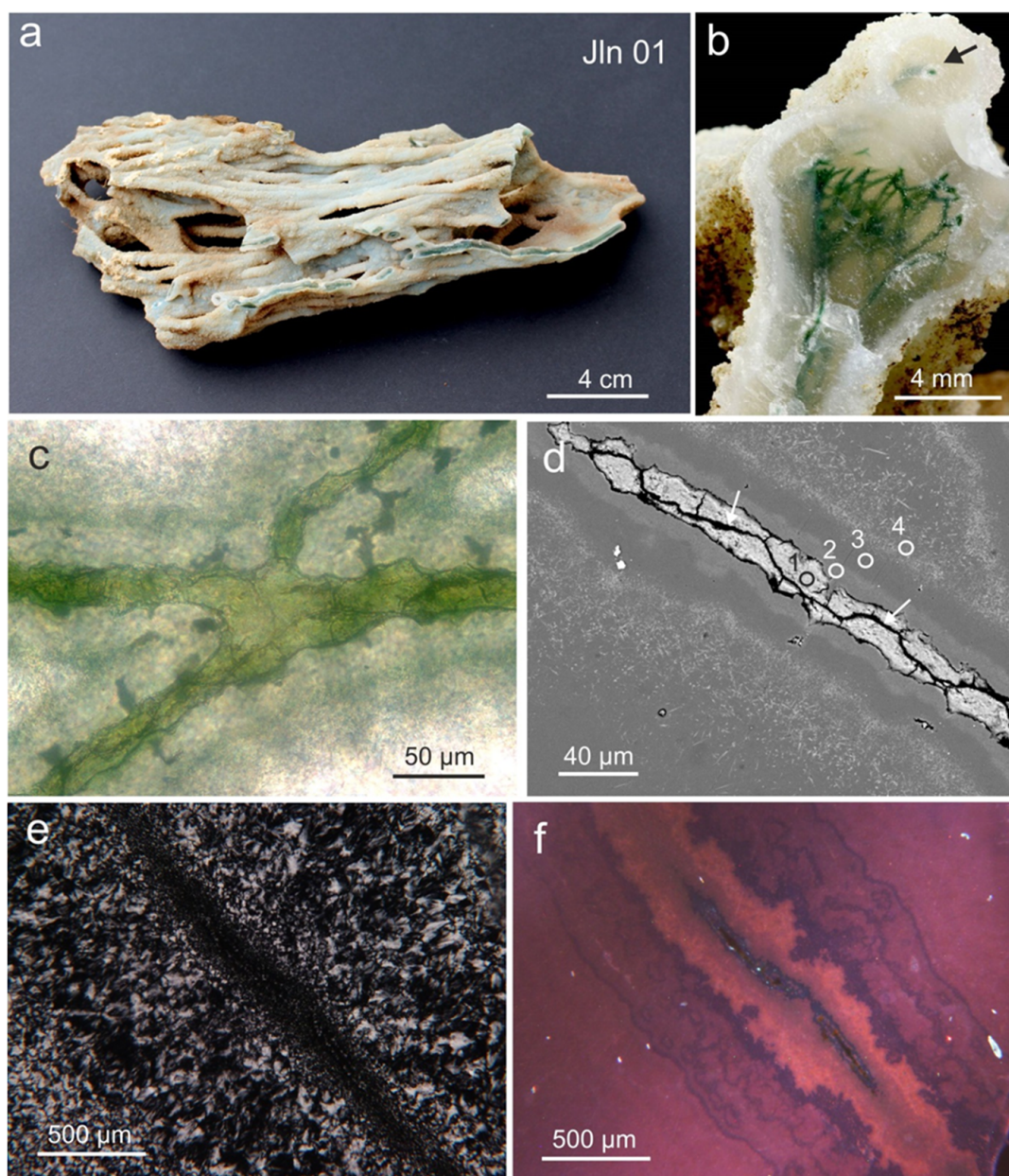


**Figure 18.** Images and micrographs showing the characteristic texture of sample Jln 01 (Jalna): (a) chalcedony aggregate consisting of a network of elongated, intergrown filamentous structures; (b) cross-section of a filamentous aggregate showing several green filamentous structures embedded in clear silica; the arrow points to the concentric structure surrounding the filamentous core; (c) transmitted light micrograph showing the internal structure of the filamentous core revealing a thin, dark green strand consisting of celadonite embedded in silica; (d) SEM-BSE image of the filamentous core; the numbers relate to measuring points of SEM-EDX analyses (for data see Table S7); the dark line in the center (see arrows) marks an empty space, which probably resulted from the former innermost filamentous core; (e,f) micrographs in transmitted light (crossed polars (e)) and CL (f) showing the non-luminescent core and different SiO<sub>2</sub> layers with varying luminescence colors.

Details of the structure show a netlike intergrowth of green filaments within a transparent silica matrix. A thin, dark filamentous core measuring ca. 10  $\mu\text{m}$  is visible within the intergrown filaments (Figure 18c). SEM investigations at high magnification revealed a zoned structure of the green filamentous cores (Figure 18d). The chemical composition of the different zones indicates

that the innermost core consists mainly of a phase having a chemical composition close to that of celadonite. Minor amounts of clay minerals (smectite?) cannot be excluded. The second zone probably represents a mixture of celadonite with  $\text{SiO}_2$  phases and is surrounded by more or less pure silica in zone 3 followed by a mixture of celadonite with silica in zone 4 (compare Figure 18d and Table S7). The black line in the center of the filament (see arrows in Figure 18d) is an empty space, which might be due to the decomposition of former (organic?) matter or shrinkage of the innermost filamentous core. Assuming filamentous bacteria as the seed for the crystallization of the following mineral layers, the decomposition of organic carbon may explain the free space.

The treatment of sample pieces with HF confirmed this zonal structure. The innermost core is removed by the chemical treatment, resulting in an empty tubular space. This channel is surrounded by a green coating, followed by numerous concentric mineralization layers of  $\text{SiO}_2$  phases, which are clearly visible due to the different solubility. The sequence of different silica zones with varying properties is also visible under cathodoluminescence (Figure 18f), which visualizes the defect structure of  $\text{SiO}_2$ . The predominantly orange-red CL is caused by the predominance of a 650 nm emission band, which indicates a high degree of disorder due to the disturbance of the regular  $\text{SiO}_4$  tetrahedral network [45].

#### 4.3. Evaluation of Possible Biosignatures in SFF

##### 4.3.1. Identification of Organic Residues in the Filamentous Cores

Investigations of three preselected and pretreated samples in the present study clearly indicate the presence of organic matter in the central filamentous core of sample Jal 11 (Jalgaon) after demineralization. The segmental micromorphology of the isolated fibers (compare Figure 11) and fluorescence after staining with Calcofluor White (CFW) (Figure 19) correlate with results reported previously for fungal chitin [46]. CFW is a sensitive fluorescent marker capable of forming hydrogen bonds with  $\beta$ -(1.4)- and  $\beta$ -(1.3)-linked polysaccharides. Previously, this staining technique was successfully used to confirm the presence of chitin in diverse living [46–49] as well as fossilized organisms [43], including chitin identified in a 505 million-year-old fossil of *Vauxia gracilenta* demosponges from the Middle Cambrian Burgess Shale [42].

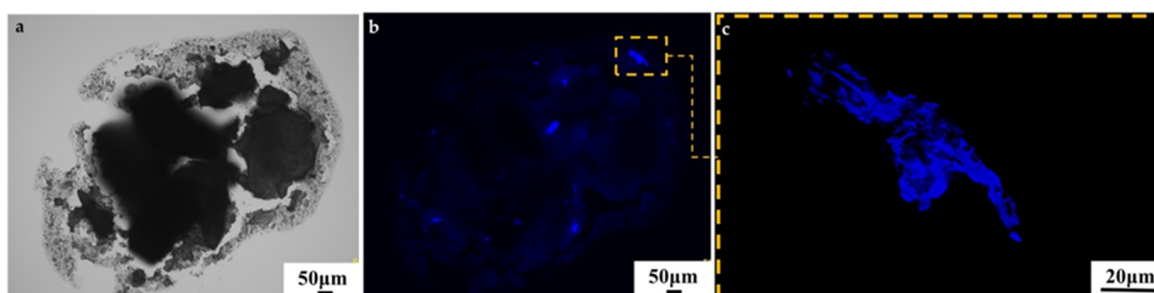


**Figure 19.** (a) Light microscopy and (b) fluorescence microscopy images of demineralized fragment of the central filamentous core of sample Jal 11 after Calcofluor White (CFW) staining (light exposure time 1/8 s.). The sample contains micro-fragments showing strong fluorescence (b,c) typical of chitin remnants.

ATR-FTIR spectra of the central filamentous core isolated from sample Jal 11 before and after demineralization are shown in Figure 20. The infrared spectra of the filamentous core prior to demineralization are typical of biosilica-based samples [50,51]. The most intense band with a maximum at  $1015\text{ cm}^{-1}$  represents the Si–O and Si–O–Si bonds [52,53]. The absorption band at  $947\text{ cm}^{-1}$  can be assigned to Si–O stretching vibrations of Si–OH groups and can often be detected in amorphous silica or marine biogenic silica [50].

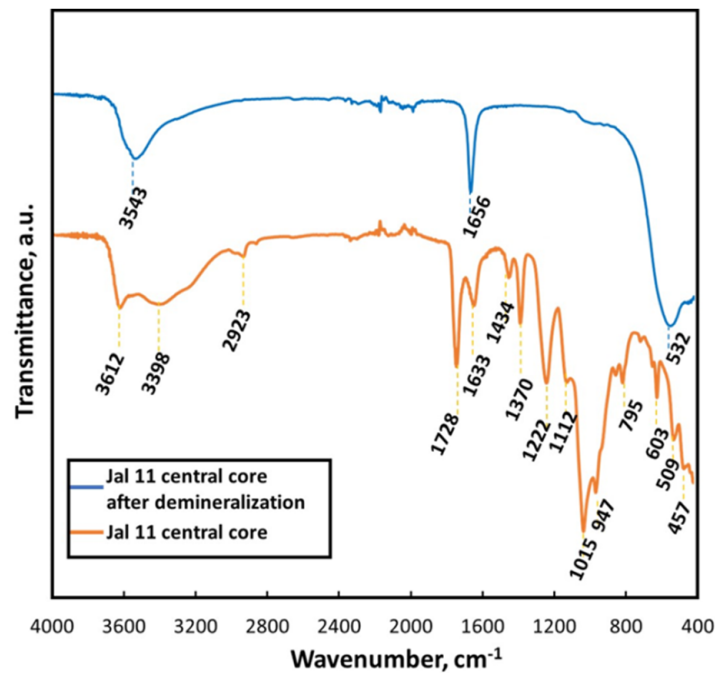


**Figure 20.** Attenuated total reflectance Fourier transform infrared spectroscopy (ATR-FTIR) spectra of the central filamentous core from sample Jal 11 before (orange line) and after (blue line) demineralization following treatment with 10% hydrofluoric acid (HF) over 4 days.

The absorption bands at 794 and 457  $\text{cm}^{-1}$  are characteristic, respectively, for symmetric stretching vibrations of Si–O–Si bonds and Si–O bending vibrations in siloxane groups [51]. The peaks visible with maxima at 3398 and 1633  $\text{cm}^{-1}$  correspond to H–O–H stretching vibrations (absorbed water) and H–O–H bending vibrations of water molecules, respectively [52,53]. Moreover, the weak band near 3612  $\text{cm}^{-1}$  is related to isolated hydroxyl groups [51].

In addition, absorption spectra show bands typical for organic matter in the spectral region between 1800 and 1300  $\text{cm}^{-1}$  [54]. The characteristic peak at 1728  $\text{cm}^{-1}$  probably belongs to C=O stretching bonds [55]. This result corresponds to the ester band in the COOH group from amino acids [54]. Additionally, the absorption bands at 1434 and 1370  $\text{cm}^{-1}$  are typical for C–H bending vibrations and may be related to methylene and methyl groups of amines. Furthermore, visible bands with a maximum at 2923  $\text{cm}^{-1}$  can be assigned to C–H stretching vibrations of methyl and methylene groups ( $\text{CH}_3$  and  $\text{CH}_2$ ) related to lipids [51]. Although HF treatment leads to significant changes in the FTIR spectra of the organic remnants, it confirms the presence of chitin. The spectrum obtained after sample demineralization (Figure 20) still represents a characteristic peak at 1656  $\text{cm}^{-1}$ , which was reported to be characteristic for amide I of chitin isolated from Basidiomycetes [56], the wood mold fungus *Aureobasidium pullulans* [57] as well as the fungus *Agaricus bisporus* [58].

The presence of chitin in the filamentous core of sample Jal 11 could be readily identified by the appearance of d-glucosamine (dGlcN) after acid hydrolysis. Under strongly acidic conditions (>6M HCl), chitin degrades to its monomer, dGlcN, which can be easily visualized by mass spectroscopy (Figure 21). This method has been utilized for chitin characterization in diverse organisms of complex chitin-based matrix organization [59–61], including chitin located within heavily mineralized skeletons of some marine sponges [62].

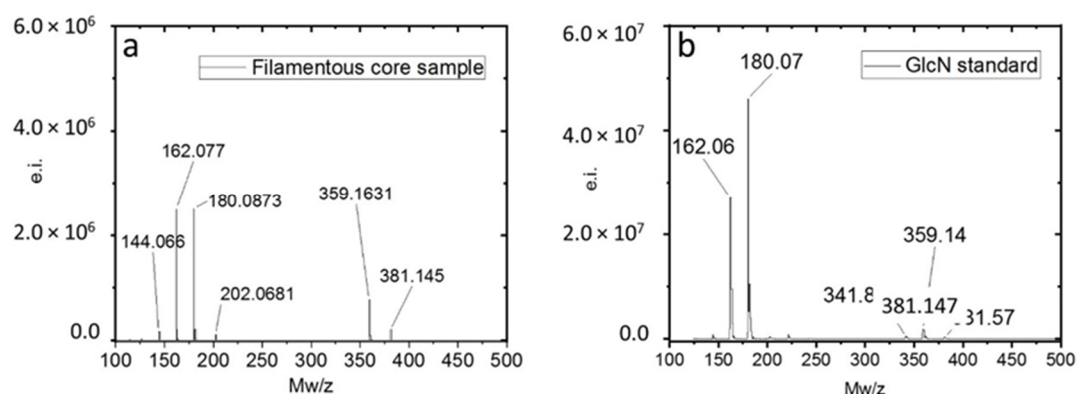


**Figure 21.** Spectra of electrospray-ionization mass spectroscopy (ESI-MS). (a) Demineralized filamentous core of sample Jal 11 after hydrolysis with 6M HCl. (b) Commercial d-glucosamine (dGlcN) standard as a positive control.

ESI mass spectrometry was also used for the identification of chitin in fossil remains [42]. The spectra of d-glucosamine show three main signals with  $m/z = 162, 180,$  and  $381$ , which correspond to the species  $(M - H_2O + H^+)$ ,  $(M + H^+)$ , and  $(M - H_2O + H^+)$ , respectively. Several other weak signals appear in which hydrogen is substituted by metal ions, commonly sodium ( $Na^+$ ). The acid hydrolysis of the demineralized filamentous core sample revealed an ESI-MS spectrum (Figure 21), which is nearly identical to the spectrum of the commercial dGlcN standard (Figure 21b). This result provides additional strong evidence for the presence of chitin within the organic remnants obtained after HF-based demineralization of the filamentous cores.

#### 4.3.2. Morphometric Analysis of Filamentous Fabrics

To constrain the origin of filamentous textures from the MDP we investigated a series of samples using optical microscopy at high magnification. All investigated samples showed a thread-like (or filament-like) center from which mineral precipitation started to form the finally macroscopic morphologies. In thin sections, or even on fractured samples, investigated using reflected light, these innermost discernible structures of the fabrics can be traced with diameters ranging from  $40 \mu m$  down to  $1\text{--}3 \mu m$ . In most examples of filamentous fabrics from the MDP, the preservation of the innermost part of the filamentous structures is rather poor, and the maximum diameter of the primary filamentous structure can be estimated at  $5\text{--}10 \mu m$ , as seen in the examples described in detail in Section 4.2. Among the samples studied by morphometry, Aur 02, Jln 01, and 31226 had the smallest innermost diameters with means of  $1.3\text{--}4.7 \mu m$ . The two measured thin sections of 31226 and Jln 01 demonstrate that the preservation in a single sample can be quite variable, depending on where a subsample for thin section fabrication is taken. In Table 2, the primary diameters assessed for the six samples selected for morphometric analysis are presented.

**Table 2.** Innermost diameters of filament structures in investigated MDP samples.

Sample	Innermost Diameter of Filaments (Mean) ( $\mu m$ )	Standard Deviation of Diameter ( $\mu m$ )	Relative Standard Deviation	Number of Filament Diameters Measured	Filament Shape Measured
Jal 17	<20	-	-	-	-
Jln 01a	1.58	0.44	0.28	19	-
Jln 01b	4.87	1.24	0.26	38	-
Jal 05	<40	-	-	-	-
Jam 17	<5	-	-	-	-
Aur 2	1.26	0.45	0.36	36	X
31226 (round)	2.36	0.90	0.38	51	X
31226 (square)	4.72	2.22	0.47	64	X

“X” marks the samples with measurements of the filament shape.

In an approach following the morphometric analysis performed for similar structures from a number of different environments [8,41], we performed additional morphometric analyses of the best-preserved specimens. The parameters measured include (i) the innermost diameter of filaments (plus absolute and relative standard deviation); (ii) tortuosity (total length/distance between start and end points), (iii) bending (degrees/micron); and (iv) direction changes (n/mm filament length). We also significantly increased the number of non-biological and biological reference samples used for comparison.

The results of this morphometric analysis are presented in Table 3. Consistent with the results of a previous study [8], the non-biological reference samples show much larger variability than the biological ones, both within a single sample and between different samples. The mean diameters range from 0.48–135  $\mu\text{m}$  for non-biological and 1.0–3.3  $\mu\text{m}$  for biological samples; the relative standard deviation (standard deviation/mean) of individual samples ranges from 0.29–1.3 (median 0.65) for non-biological and 0.10–0.30 (median 0.16) for biological samples. Values of tortuosity, bending, and direction changes are also typically higher in biological samples. The two MDP samples analyzed show values for these morphometric parameters generally similar to the biological filaments. The variability of the measured diameters is higher than for most biological samples, but this parameter is likely affected by mineral precipitation on the original structures.

**Table 3.** Filament morphometry data of MDP filamentous samples compared with biogenic and abiogenic samples; the numbers in brackets in (d) show the number of measurements.

Samples	Diameter ( $\mu\text{m}$ )	Standard Deviation	Bending ( $^\circ/\mu\text{m}$ )	Direction Changes (mm)	Biogenicity (%) <sup>1</sup>
<b>(a) Abiogenic reference samples (23 samples, 1840 diameters, 345 shapes)</b>					
Mean	15.0	0.72	0.27	2.37	
Median	5.6	0.66	0.08	0.03	
Minimum	0.5	0.29	0.00	0.00	
Maximum	134.6	1.40	1.66	21.0	14
<b>(b) Biological reference samples (17 samples, 830 diameters, 266 shapes)</b>					
Mean	2.1	0.17	1.74	44.78	
Median	2.0	0.16	0.71	15.80	
Minimum	1.0	0.10	0.31	5.90	
Maximum	3.3	0.30	15.40	344.00	100
<b>(c) Biogenicity criteria</b>					
	1.0–3.4	<0.43	>0.30	>5.0	
<b>(d) Samples from the Deccan trap basalts</b>					
31226 moss agate a	4.70	0.47 (64)	0.34	10.3 (21)	50
31226 moss agate b	2.40	0.38 (51)	0.83	21.5 (8)	100
Aur01 filamentous	1.26	0.36 (36)	1.26	44.3 (22)	100
Jln01 filamentous fabric <sup>2</sup>	1.58	0.28 (19)	1.13	48.8 (7)	75
	4.90	0.26 (38)			

<sup>1</sup> % of parameters (mean values) classified as biogenic-based criteria defined under (c); for the 23 abiogenic reference samples, 13 out of 92 averaged parameters classify as biogenic (14%); for the 17 biogenic reference samples, 68 out of 68 averaged parameters classify as biogenic (100%). <sup>2</sup> Data for diameters are for two different parts of the analyzed sample.

## 5. Discussion

### 5.1. Chemical Development and Mineralization Sequence of SFF

The low viscosity of compound lavas in the DVP causes high porosity and the development of large cavities in the tholeiitic basalts. This is an important precondition for fluid mobility and results in the precipitation and crystallization of secondary minerals in the amygdales. All elements necessary for mineral formation, such as Si, Mg, Al, and Fe were released during alteration of the volcanic host rocks and supplied by the percolating fluids. The chemical composition of the fluids reflects the interaction of the host rocks with hydrothermal fluids of meteoric and possibly magmatic origin [5] and

shows characteristic development trends, which provide information about the formation conditions of the SFF.

Investigations of the cross-sections of the filaments provided more details about the crystallization process. The first mineralization sequence is mostly composed of Fe-rich compounds, and partially elevated amounts of carbon could be detected. This organic carbon might be an indication of microbial activity during the early formation stage. Observations of numerous samples from the Savda quarries [5] have shown that, in particular, clay minerals were formed during the early crystallization process and often constitute the cores of the SFF. In general, clay minerals (sheet silicates) represent the most significant alteration minerals both in natural and laboratory-confirmed alteration of volcanic rocks [63–67].

The formation of celadonite and smectites preferentially occurs under neutral to alkaline pH conditions, but sometimes also in a weakly acidic environment [65]. The chemical composition of celadonite is often heterogeneous and may show varying Fe–Al–Mg–Si ratios as well as K content. Such chemical heterogeneity can also be observed for minerals of the smectite group, resulting in differentiation of an Fe-poor and Fe-rich subgroup [67]. A representative Fe-rich smectite is Fe-bearing saponite (magnesioferrosaponite), which is preferentially formed during the low-temperature alteration process of basaltic rocks [65,67]. In addition, laboratory experiments of volcanic glass and diabase at 150 °C confirm the smectite formation [63]. Within the secondary mineral sequences in the cavities of the Savda basalts no other minerals with significant Fe or Mg content were detected that formed after the clay minerals [5].

The next mineralization step is characterized by different zeolites (e.g., heulandite, stilbite, and mordenite). The composition of the volcanic host rocks provide a large quantity of Ca, leading to the crystallization of Ca-rich zeolites. These zeolites crystallize at temperatures of ca. 100 °C. Such temperature conditions are also confirmed by results of fluid inclusion studies in associated calcite, which provided homogenization temperatures between 101 and 157 °C [5]. The increasing amount of SiO<sub>2</sub> in the mineralizing fluids first results in the formation of mordenite, the zeolite mineral with the highest SiO<sub>2</sub> content, and subsequently the formation of pure silica minerals.

The precipitation of silica minerals often begins directly at the surface of the filamentous core. Sometimes, the precipitation of silica has encrusted crystals of previously formed mordenite or clay minerals. The thickness of the crust can vary between 1 and 20 mm and most filaments are completely protected by a chalcedony crust. The presence of opal-CT, cristobalite, chalcedony, and macro-crystalline quartz as well as the outwards increasing crystal size are strong indications that silica minerals formed through several structural states of SiO<sub>2</sub> with amorphous silica as the first solid phase.

The observed “Bambauer quartz” (Figure 7) can provide additional information about physicochemical conditions during crystallization of quartz. A low temperature hydrothermal environment with variations in pH/T conditions as well as strong fluctuations in silica concentration results in the formation of such characteristic growth lamellae [68] and is most likely responsible for the varying appearance of different silica phases within the SiO<sub>2</sub> aggregates. The results of CL studies strongly indicate the existence of several SiO<sub>2</sub> generations (Figures 7 and 18).

## 5.2. SFF Micro-Structure

Two general types of SFF could be distinguished based on their macroscopic appearance and filament morphology. The first type is characterized by straight to curved linear filaments or filament intergrowths with a round cross-section (SFF<sub>Ir</sub>; Figure 2a,b). In the case of gravity-controlled growth, the filaments develop shapes resembling stalactites. It is remarkable that the external diameter of these SFF in general does not change over the total length ranging from a few millimeters up to more than 100 cm. The second type can be characterized as planar matted fabrics of irregularly intergrown strands (SFF<sub>Ma</sub>; Figure 2c).

The cross-sections of SFF<sub>Ir</sub> display basically four different main zones: (1) core zone, (2) empty tube zone, (3) zeolite zone, and (4) outer silica zone (Figure 22). The core zone consists of an innermost

filamentous core with diameters between 1 and 50  $\mu\text{m}$  and a surrounding clay mineral zone. If iron hydroxides or oxides are present, they may form the innermost filament with a diameter of 1 to 5  $\mu\text{m}$ . However, such a core is rarely preserved, and the core zone consists entirely of clay minerals. The diameter of the clay mineral core ranges from 30 to 50  $\mu\text{m}$ , or in extreme cases up to 200  $\mu\text{m}$ . Based on the analytical results, the sheet silicates can be related to the mica group (celadonite) and/or to the smectite group (saponite and montmorillonite). Depending on the mineral composition, the color varies from intense green, olive-green or brown to nearly black. It is noteworthy that the composition of the clay minerals of the SFF is identical to that of the wall lining clay minerals in the same cavity. In general, Fe-rich clay minerals dominate, but in some SFF Fe-poor montmorillonite is also detected.

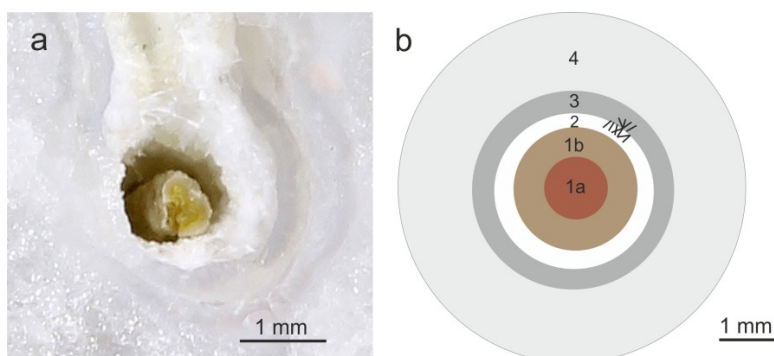


**Figure 22.** (a) Cross-section of sample Jal 11 and (b) schematic microstructure of  $\text{SFF}_{\text{Ir}}$ : 1a = filamentous core (Fe-rich sheet silicates), 1b = outer part of the filament core (Fe-containing sheet silicates), 2 = surrounding zone of an empty tube (partially containing fibrous zeolite, e.g., mordenite), 3 = zeolite zone, 4 = marginal zone consisting of a 0.5–20 mm thick zone of silica minerals.

The following mineralized zone consists of minerals of the zeolite group, predominantly mordenite. In addition, other zeolites such as heulandite/clinoptilolite and stilbite were detected close to the growth base of the  $\text{SFF}_{\text{Ir}}$ . The zeolites crystallized at the outer surface of the clay minerals of the core zone and were subsequently overgrown by the early  $\text{SiO}_2$  phases. In several  $\text{SFF}_{\text{Ir}}$ , the zeolite zone is missing and instead a transition zone with clay minerals included in the early silica assemblage formed. On the other hand, a remarkable tube-like gap is often developed between the clayey filament core and the zeolite zone, which can contain euhedral zeolite crystals such as needle-like mordenite (compare Figure 10). The unhampered growth of zeolites indicates a free space, which might have developed due to shrinkage (or dissolution) of the clay minerals from the filamentous core (e.g., swellable smectite minerals).

The  $\text{SiO}_2$  mineralization starts as amorphous silica, followed by opal-CT, cryptocrystalline chalcedony, and macro-crystalline quartz. Clay minerals and/or zeolites can be imbedded in an early stage of the silica precipitation. As a result of progressive precipitation, the silica zone commonly develops into a more or less round cross-section of the  $\text{SFF}_{\text{Ir}}$  and may enclose one or more filaments. Thus, one  $\text{SFF}_{\text{Ir}}$  can contain several core zones, which are directly connected or included in a united silica layer. The diameter of the  $\text{SFF}_{\text{Ir}}$  depends on the number of included core zones and more importantly on the thickness of the silica assemblage, which can reach more than 1 cm.

$\text{SFF}_{\text{Ma}}$  often form a network of elongated, intergrown filaments included in chalcedony. The cross-section of single filaments shows an innermost filamentous core consisting of celadonite or other sheet silicates (Figure 23). The core is embedded in a mixture of celadonite and silica followed by a layer of pure silica (Figure 23). The thickness of the layers commonly reaches a few millimeters. If cavities are partly or completely filled by  $\text{SFF}_{\text{Ma}}$ , complex three-dimensional matted masses are developed, described as moss agate. The core filaments do not form parallel or similar intergrowths like the  $\text{SFF}_{\text{Ir}}$ . In fact, intergrowths are characteristic in individual threads that are connected at varying angles to each other and develop matted aggregates (Figures 2c and 23).

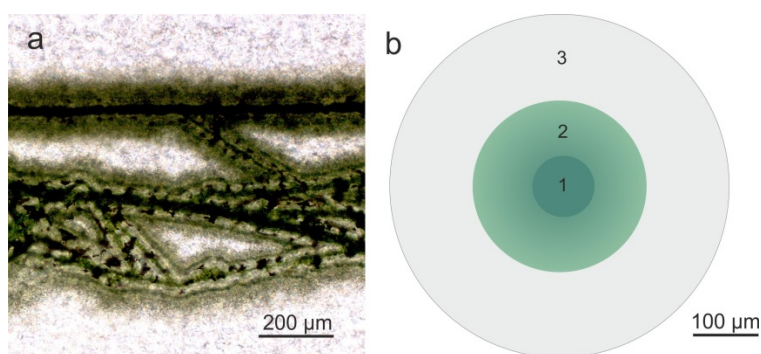


**Figure 23.** (a) Microstructure of sample Jln 01; (b) schematic cross-section of SFF<sub>Ma</sub>: 1 = filamentous core consisting of sheet silicates (e.g., celadonite), 2 = chalcedony intergrown with sheet silicates, 3 = pure SiO<sub>2</sub>.

The detailed morphometric analysis revealed that the typical micro-textures observed in the filamentous fabrics from the MDP are clearly distinct from similar types of non-biological aggregates such as fibrous minerals, speleothems (stalactite-type) or inorganic precipitates similar to “chemical gardens” [69–71].

Fibrous minerals as an origin can be excluded with certainty based on the strong differences seen among the morphometric parameters (compare Table 3). In particular, the mineral fibers display much larger variability in their diameters, the fibers are typically straight (low tortuosity) and show low degrees of bending and small numbers of direction changes (Table 3). In accordance with data from the literature, no examples of fibrous minerals could be found that show the same morphological characteristics as the filamentous fabrics.

Speleothems, including excentriques, can show a range of morphologies similar to the filamentous fabrics described here. However, true stalactites are characterized by a central channel that is the size of a drop of water and have much larger diameters. Excentriques lack both the vertical orientation (by definition) and mat-like two-dimensional elements.

Chemical garden-like precipitates are referred to by some authors [72–75] as explanations for filamentous fabrics of both synthetic and natural origin and are similar to those described in this work. We investigated two lines of evidence: morphometry and conditions of formation. The morphometric analyses performed in this work show that the analyzed chemical garden precipitates show similarities in the parameters’ “bending” and “number of direction changes”, while the diameters of filamentous shapes from chemical garden experiments show a much larger variability than biological filaments, expressed as the relative standard deviation of the mean diameter (0.58, 1.30, 1.40) for our chemical garden samples and 1.51 for chemical garden samples described in McMahon [75], while the mean values of the relative standard deviation for biological filaments range from 0.10 to 0.30 (median 0.16,  $n = 17$ ). Considering the conditions of formation, intrinsically chemical gardens are products resulting from extreme chemical disequilibria (classically soluble heavy metal salt crystals in contact with alkali silicate solutions at extremely high pH, e.g., Pagano et al. [70]), a situation difficult to invoke for environments of lava flows interacting with near-surface groundwater. In particular, the vertical orientation observed in chemical gardens is based on the density difference between alkaline silicate solution and less dense heavy metal solutions rising from dissolving metal salt grains. The vertical orientation in chemical gardens thus heavily relies on the high concentration of the silicate solution, a product that has never been observed in nature and is highly unlikely to form due to the extreme conditions required. McMahon [75] showed that filament-like forms can be experimentally obtained even in the absence of silicate solutions, in sodium carbonate solutions brought to pH 7 using hydrochloric acid (i.e., a neutral sodium chloride solution). Abundant and macroscopically visible filament-like forms are not typically formed from just ferrous salts in aqueous solutions at

neutral pH but are characteristic of the alkali-silicate-rich systems typically constituting chemical garden experiments.

In summary, we found that the geometry of filamentous fabrics constituting the skeleton of mineral precipitates in the Deccan trap basalts does not correspond to the geometry of mineral fibers, inorganic speleothems, and products of chemical garden-type reactions. The filamentous fabrics are similar to microbial filaments and fabrics made up of these and thus, are most likely initiated by microbial communities active in these cavities.

### 5.3. Biogenic Origin and Formation Mechanism of SFF

Altered rocks and sediments in oceans as well as in surface and subsurface environments are the most common and widely distributed habitats of bacteria in geological settings. Numerous studies have shown that both rock alteration and mineral formation due to microbial activities are possible, even under extreme conditions [76–79]. In particular, the common tubular alteration of basaltic glass in submarine environments was attributed by several authors to microbial boring as euendoliths and interpreted as evidence of biogenicity, but this was also critically debated [80–86]. However, such suggested bioalteration tubes observed in altered volcanic rocks represent negative forms resulting from the corrosion of glass and therefore, have a different mode of origin than SFF, which represent positive shapes that formed in cavities and were encrusted by aqueous deposition of minerals.

SFF from the Deccan Volcanic Province are particularly spectacular as they are unusually large, wide-spread, and associated with striking crystals of younger hydrothermal minerals that allowed the detailed elucidation of hydrothermal processes postdating the initial formation of SFF [5]. Texturally similar SFF are also known from other volcanic provinces [8,87], but from very different environments, such as the oxidation zone of ore deposits [41,88,89], karst environments [90,91], and low-temperature hydrothermal veins [92]. The geological conditions in the DVP point to the partly long-lasting cooling of effused lava before burial and cover by new lava flows resulting in temperatures below 100 °C and atmospheric pressure, both favorable conditions for the life of organisms [93].

Detailed investigations of the SFF showed that the innermost filamentous core often consists of thread-like, mostly Fe-rich sheet silicates (Fe-rich saponite and celadonite). The detected relics of organic matter and the partly analyzed excess carbon indicate that these inner filaments might be the result of biochemical activities. This is supported by results of morphometric characterization of filamentous micro-textures, which are remarkably different from inorganic mineralization (fibrous minerals, stalactitic growth, and chemical gardens).

Whereas stalactites are characterized by a mono-mineral composition, the filamentous fabrics in the DVP constitute a polyphase mineral assemblage, which is often identical with the mineralization sequence on the cavity walls. The main arguments against stalactitic growth of SFF are their variable morphologies but small innermost cross-sections of 1–50 µm. Moreover, processes similar to those resulting in the development of chemical gardens (self-assembling) cannot be considered for the formation of SFF. The high Na and Si content in the fluid required for such a process [94,95] is very unlikely to be provided during alteration of basalt. According to Kellermeier et al. [96] the growth of silica biomorphs is favored at pH values between 9.3 and 9.8 in gels and between 10.2 and 11.1 in solutions and the morphology is mainly influenced by other parameters such as temperature or different cations. This is in disagreement with the results of the present study, which strongly indicate circumneutral pH conditions and maximum temperatures of 120 °C.

The geometric properties of the filamentous fabrics forming the substrates for hydrothermal mineral precipitation in cavities of the Deccan trap basalts are consistent with an origin resulting from the mineralization of microbial fabrics based on filaments, followed by the abiotic precipitation of a complex assemblage of minerals [5]. The biological origin of the filamentous textures is indicated by the following qualitative arguments: (i) evidence for flexibility including vertical orientation and U-loops; (ii) frequent formation of sheet-structures (mats) formed by many filaments; (iii) the fact that the filamentous textures represent the earliest formation in cavities, formed prior to a long sequence of

mineral precipitation and deep burial; (iv) ubiquitous presence of iron-rich phases, iron hydroxides being replaced by later iron silicates, among the earliest precipitates making up the filamentous textures; this is consistent with the activity of iron oxidizing microbial communities followed by mineral precipitation at elevated temperatures with partial replacement of early iron hydroxides by iron silicates.

Quantitative arguments for a biological origin of the filaments that constitute the innermost skeleton of the fabrics are provided by the morphometric analysis of the filaments. We have shown that the following morphometric parameters of the filamentous fabrics are consistent with the same parameters that were obtained from certain microbial filaments, while they are strongly different from the same parameters as obtained from a range of non-biological filament-like objects: diameter of the innermost filaments; variability of the diameter of the innermost filaments; tortuosity; degree of bending; number of direction changes (compare Table 3).

The existence of specific morphological characteristics of biological filaments has recently been assessed by several studies [87,97,98]. The occurrence of SFF in different environments demonstrates that their formation is unrelated to the specific conditions prevailing in these environments, but consistent with the widespread presence of microbial life in subsurface environments. Therefore, our conclusion is that the SFF from the Deccan Volcanic Province are likely of biological origin. Alternative explanations of origin would require modes of filament formation currently unknown to science.

The detection of chitin remnants, most likely of fungal origin, was the first direct evidence for organic residues in the investigated SFF. Such fine fungal filaments could have acted as the initial nucleus (biogenic template) and initiated the mineralization processes. Perry et al. [99] introduced the term organominerals, which is applied to minerals that are affected by mostly life-related organics, but not directly produced by living cells (i.e., induced mineralization because of nucleation on organic surfaces acting as seeds, element supply, and/or physicochemical conditions). However, recent studies have also evidenced the active biomineralization potential of fungi. Certain results revealed the participation of fungi during jarosite mineralization under acidic conditions (*Purpureocillium lilacinum*), carbonate mineralization governed by calcifying fungi (*Aspergillus sp. UF3*; *Fusarium oxysporum UF8*), and formation of nano-scale minerals such as montmorillonite and goethite in soils (*Aspergillus fumigatus Z5*) [100–103]. In this context, the montmorillonite filament in sample Jal 11 could be the result of such biological processes.

Bioformation of amorphous clay minerals, nontronite or montmorillonite can also be related to microbial processes [104–106]. The bio-compounds strongly affect the acceleration and retardation of chemical reactions running under slightly acidic to neutral conditions at temperatures between 20 and 70 °C. The type of assemblage formed depends on a number of biogeochemical factors, such as temperature, pH, Eh, dissolved oxygen concentration, electrical conductivity, and/or element supply [104]. In general, bacterial cell walls may act as favorable interfaces for the binding of metal ions and subsequent mineral growth [107]. Several models have been developed concerning the initial stages of phyllosilicate formation triggered by microorganisms.

Natural observations and laboratory experiments have shown that organic activity might be associated with fine-grained (Fe, Al) silicates (in particular clay minerals), which develop due to adsorption of cationic iron to anionic cellular surfaces and subsequent precipitation of a precursor ferric hydroxide phase. The subsequent reactions with dissolved silica and aluminum result in the formation of an amorphous precursor phase with clay-like compositions between allophane and chamosite showing no electron diffraction patterns [108,109]. Alternatively, the colloidal (Fe, Al) silicate compounds may react directly with the cellular surface or the adsorbed iron and convert to stable crystalline phases during dehydration of the hydrous precursor. The transformation of such metastable phases (e.g., hydroxy-aluminosilicate (HAS)) into more stable phases occurs under saturated conditions and is controlled by inherent thermodynamic properties of saturated minerals in the fluids and by abiotic mineralization [110]. The Si binding and silicate formation may be a result of binding of Si anions either to positively charged sites of the cell wall, such as amine groups, or through bridging

by metal ions bonded with negatively charged sites at the cell surface such as carboxyl ( $\text{COO}^-$ ) or phosphoryl groups ( $\text{PO}_3^{2-}$ ) [111].

Biomineralization is also known from certain iron and manganese oxidizing bacteria such as *Gallionella* or *Leptothrix*, which actively or passively accumulates elements from its environment for metabolic use resulting in the precipitation of mineral encrustations [112,113]. During these processes, the stalk of *Gallionella* may become heavily encrusted with iron-oxyhydroxide or the filaments of *Leptothrix* by Fe- or Mn-oxides. For instance, Chan et al. [114] observed highly elongated filaments of iron-oxyhydroxide (akaganeite) on polysaccharide strands extruded by the cell. On the other hand, several microorganisms such as various hyperthermophilic archaea (*Geobacter spp.*, *Shewanella spp.*, *Albidiferax ferireducens*, *Geothrix fermentans*) can also reduce  $\text{Fe}^{3+}$  under reducing conditions using certain electron donors such as acetate, lactate, and/or  $\text{H}_2$  [112].

Such microbially mediated reactions may occur at low oxygen concentration and simultaneous abiotic oxidation at high  $\text{O}_2$  concentration. Microbial  $\text{Fe}^{2+}$  oxidation to  $\text{Fe}^{3+}$  for obtaining energy runs initially at circumneutral pH and at elevated temperatures (e.g., *Gallionella ferruginea*), and the  $\text{Fe}^{3+}$  mineral products provide surface sites for subsequent autocatalytic abiotic reactions. It is very likely that some proteins pump out the ferric iron to prevent the precipitation of iron oxyhydroxide in the bacteria interior resulting in the encrustation of the microbes [111]. Typical mineral products are fibrous ferrihydrite, lepidocrocite, and akaganeite, which are partly unstable and can subsequently be transformed to iron oxides/hydroxides. Alternatively, the iron compounds can be incorporated into Fe-rich sheet silicates [115,116].

Bacteria with a stalk- or sheath-like morphology such as *Gallionella spp.* or *Leptothrix ochracea* can form characteristic thread strands with lengths of more than 100 cm and a diameter of up to 50  $\mu\text{m}$ , which consist of numerous accumulated strands [113]. As a result, the microstructure of micro-tubes composed of fine, frequently folded, clay sheets shows close similarity in size and form to sheath-forming bacteria [105]. Investigations of the iron-bearing fabrics of the innermost SFF cores at high magnification do not reveal the presence of characteristic crystal shapes, but a morphology resembling that of bacteria filaments. Therefore, we assume that the SFF in the cavities of DVP basalts from Savda exhibit features of a biogenic signature.

The subsequent overgrowth of initial biogenic filaments by ferrihydrite and/or the following transition to Fe-rich phyllosilicates such as celadonite or smectite resulted in an increase in the SFF density. As a consequence, the heavy SFF sank to the cavity bottom or could be connected to the cavity walls and formed random intergrowths. Only gravity-controlled SFF survived as long linear individuals. We assume that these early processes of filamentous core formation, the precipitation of iron compounds as well as crystallization of Fe phyllosilicates occurred after cooling of the lava in a sub-surface environment. The further overgrowth by mordenite and the final encrustation by silica minerals happened later during progressive burial and within a long period of up to several thousands of years.

## 6. Conclusions

Complex investigations of SFF from the Deccan Volcanic Province (DVP) in India have shown that different types of these spectacular aggregates exist. Despite the variations in micro-texture and mineral assemblages, general trends in geochemical evolution and mineralization sequences have been detected.

The main outcome of this study is the first direct evidence for organic residues in the SFF mineralization. Detailed investigations of the innermost parts of the SFF revealed fungal chitin in the filamentous core. Such fine fungal filaments could have acted as initial nuclei (biogenic template) for the mineralization processes. Moreover, several studies have shown an active biomineralization potential of fungi, for example, for the formation of smectite. In the DVP samples, the residues of fungal chitin were detected within filament strands mainly consisting of montmorillonite and therefore strongly indicate biochemical processes at least during an early stage of SFF mineralization.

In addition, the morphometric characteristics of certain filamentous fabrics are very similar to those of microbial filaments and fabrics made up of these, providing additional support for the hypothesis that microbial communities were active during SFF formation in the basaltic cavities. The different shapes of the SFF, ranging from gravity-controlled straight forms resembling stalactites to branching aggregates, might be the result of microbial activity and reflect the specific conditions during primary growth.

Supported by the specific geological and geochemical conditions in the compound lava flows of the DVP, a characteristic mineralization sequence developed on the filamentous nucleus. The sequence normally started with Fe-rich phases (probably Fe-oxides/-hydroxides, Fe-rich sheet silicates such as celadonite and smectite-saponite), continued with Ca-rich zeolites and finished with a cover of different SiO<sub>2</sub> minerals (opal-CT, chalcedony, and macro-crystalline quartz). The fluids percolating the volcanic rocks provided all the released elements from the alteration of the host rocks such as Si, Mg, Al, and Fe that are necessary for mineral formation. The large size of cavities and high porosity of the surrounding host rocks ensured a continuous and long-lasting fluid flow and supply of material. As a result, the cross-sections of SFF display similar concentric layers of the mineral succession and reach thicknesses of several centimeters and spectacular lengths of up to 100 cm with constant diameters.

Assuming microbial activity during the beginning of SFF formation, the upper temperature limit of initial SFF formation probably was 100–120 °C. These temperatures are in accordance with formation temperatures of zeolite minerals and homogenization temperatures of fluid inclusions in quartz and associated calcite. The early crystallization of zeolites such as mordenite indicates neutral or slightly alkaline mineralization conditions changing to slightly acidic conditions during silica precipitation. The observed mineralization sequence points to temporal variations in the chemical composition of the mineralizing fluids from Fe-rich to Ca dominated and finally pure SiO<sub>2</sub>. Textural features such as variations in mineral morphology, “Bambauer lamellae” in quartz or different chalcedony layers indicate fluctuations in the specific pH/T conditions during SFF growth. The sporadically observed apophyllite as overgrowth on SFF may be related to later separate hydrothermal processes at higher temperatures.

Based on the field observations and the analytical results of the study, SFF formation in the DVP can be ascribed to three main mineralization stages: (1) formation of very tiny filaments (predominantly Fe compounds, smectite, and/or celadonite) with diameters of ca. 1 µm, possibly initiated or governed by fungal/microbial activity; (2) encrustation of the filamentous cores by subsequent mineralization of sheet silicates and zeolites accompanied by an increase of the diameter up to 20–50 µm; (3) final SFF formation due to encrustation and cementation of one or more filamentous cores by silica minerals resulting in diameters up to several centimeters and lengths of several tens of centimeters.

The abundance of large, easily recognizable SFF in cavities of DVP basalts demonstrates that subsurface microbial life may result in macroscopic expressions in mineralized form. The presence of SFF may thus be used to infer the possible former presence of subsurface life not only in different types of terrestrial rocks, but potentially also in geologically similar situations on other planetary bodies such as Mars.

**Supplementary Materials:** The following are available online at <http://www.mdpi.com/2075-163X/10/6/540/s1>, Table S1: Results of local chemical analyses (SEM-EDX) of celadonite, mordenite, and the filamentous core of SFF in samples from Jalgaon/Savda, India. The locations of the analytical points FC2 and FC3 in sample Jal 33 are shown in Figure 10d; Table S2: Results of local chemical analyses of core filaments in sample Jal 11 by SEM-EDX. Z refers to zeolite (mordenite) and S to smectite; the analytical points of Z1 and S1 are shown in Figure 11e; Table S3: Results of local chemical analyses (SEM-EDX) of selected areas of the filamentous core in sample Jal 05 (analytical spots are shown in Figure 13c); Table S4: Results of SEM-EDX analyses of the innermost filamentous core of sample Jal 5m 01 (for analytical spots compare Figure 14d) as well as smectite (Figure 14f); Table S5: Results of SEM-EDX measurements of selected areas of the filamentous core of sample Jam 01 (for analytical spots compare Figure 16c); Table S6: Results of local chemical analyses of zeolite/mica minerals in the filamentous core of sample Jam 10 by SEM-EDX; Heu = heulandite/clinoptilolite (Figure 17c); Cel = celadonite (Figure 17e), Mor = mordenite (Figure 17d); Stil = stilbite (Figure 17f); Table S7: Results of SEM-BSE analyses showing the chemical composition of different filament zones in sample Jln 01 (Jalna, compare Figure 18d); 1 = celadonite, 3 = silica; 2, 4 = mixture of celadonite and silica.

**Author Contributions:** B.O. collected the studied samples and provided the geological data. J.G., B.H., T.M., M.V.T., T.J., H.E., R.K. conducted different analytical measurements, evaluated the mineralogical and geochemical data, and provided appropriate parts of the manuscript. J.G. and B.O. compiled and wrote the final version of the manuscript. All authors have read and agreed to the published version of the manuscript.

**Funding:** This research received no external funding.

**Acknowledgments:** We would like to thank Christian Rewitzer (Furth im Wald) for his support with SEM/EDX analyses, and Jessica Gärtner and Tina Wesiger (TU Bergakademie Freiberg) for assistance during analytical work. The reviews of two anonymous reviewers and the Academic Editor, as well as Thomas Monecke (Colorado School of Mines) improved the quality of the paper significantly.

**Conflicts of Interest:** The authors declare no conflict of interest.

## References

- Hofmann, B.A. Subsurface filamentous fabrics. In *Encyclopedia of Geobiology*, Dordrecht; Reitner, J., Thiel, V., Eds.; Springer: Berlin/Heidelberg, Germany, 2011; pp. 851–853. [\[CrossRef\]](#)
- Sukheswala, R.N.; Avasia, R.K.; Gangopadhyay, M. Zeolites and associated secondary minerals in the Deccan Traps of Western India. *Miner. Mag.* **1974**, *39*, 658–671. [\[CrossRef\]](#)
- Ottens, B. Die drusenmineralien aus dem spilitbasalt von Bombay/Indien. *Der Aufschluß* **1998**, *49*, 133–149.
- Ottens, B. Minerals of the deccan traps India. *Miner. Rec.* **2003**, *34*, 1–82.
- Ottens, B.; Götze, J.; Schuster, R.; Krenn, K.; Hauzenberger, C.; Zsolt, B.; Vennemann, T. Exceptional multi stage mineralization of secondary minerals in cavities of flood basalts from the Deccan Volcanic Province, India. *Minerals* **2019**, *9*, 351. [\[CrossRef\]](#)
- Morteani, G.; Kostitsyn, Y.; Preinfalk, C.; Gilg, H.A. The genesis of the amethyst geodes at Artigas (Uruguay) and the paleohydrology of the Guaraní aquifer: Structural, geochemical, oxygen, carbon, strontium isotope and fluid inclusion study. *Int. J. Earth Sci.* **2009**, *99*, 927–947. [\[CrossRef\]](#)
- Hofmann, B.A.; Farmer, J.D. Filamentous fabrics in low-temperature mineral assemblages: Are they fossil biomarkers? Implications for the search for a subsurface fossil record on the early Earth and Mars. *Planet Space Sci.* **2000**, *48*, 1077–1086. [\[CrossRef\]](#)
- Hofmann, B.A.; Farmer, J.D.; Von Blanckenburg, F.; Fallick, A.E. Subsurface filamentous fabrics: An evaluation of possible modes of origins based on morphological and geochemical criteria, with implications for exopalaeontology. *Astrobiology* **2008**, *8*, 87–117. [\[CrossRef\]](#)
- Sheth, H.C. Flood basalts and large igneous provinces from deep mantle plumes. *Tectonophysics* **1999**, *311*, 1–29. [\[CrossRef\]](#)
- Sheth, H.C. Large Igneous Provinces (LIPs): Definition, Recommended Terminology, and a Hierarchical Classification. *Earth-Science Reviews* **2007**, *85*, 117–124. [\[CrossRef\]](#)
- Subbarao, K.V. *Deccan Volcanic Province*; Geological Society of India: Bangalore, India, 1999.
- Pande, K. Age and duration of the deccan traps, India: A review of radiometric and palaeomagnetic constraints. *Proc. Indian Acad. Sci. Earth Planet Sci.* **2002**, *111*, 115–123. [\[CrossRef\]](#)
- Sheth, H.C. The deccan beyond the plume hypothesis. *Geophys. Res. Abstr.* **2006**, *8*, 2.
- Chenet, A.L.; Courtillot, V.; Fluteau, F.; Gérard, M.; Quidelleur, X.; Khadri, S.F.R.; Subbarao, K.V.; Thordarson, T. Determination of rapid Deccan eruptions across the Cretaceous-Tertiary boundary using paleomagnetic secular variation: 2. Constraints from analysis of eight new sections and synthesis for a 3500-m-thick composite section. *J. Geophys. Res. Solid Earth* **2009**, *114*, 1–38. [\[CrossRef\]](#)
- Keller, G.; Adatte, T.; Gardin, S.; Bartolini, A.; Bajpai, S. Main Deccan volcanism phase ends near the K–T boundary: Evidence from the Krishna–Godavari Basin, SE India. *Earth Planet. Sci. Lett.* **2008**, *268*, 293–311. [\[CrossRef\]](#)
- Bondre, N.R.; Duraiswami, R.A.; Dole, G. Morphology and emplacement of flows from the Deccan Volcanic Province, India. *Bull. Volcanol.* **2004**, *66*, 29–45. [\[CrossRef\]](#)
- Vanderkluisen, L.; Mahoney, J.J.; Hooper, P.R.; Sheth, H.; Ray, R. The Feeder System of the Deccan Traps (India): Insights from Dike Geochemistry. *J. Pet.* **2011**, *52*, 315–343. [\[CrossRef\]](#)
- Keller, G.; Sahni, A.; Bajpai, S. Deccan volcanism, the KT mass extinction and dinosaurs. *J. Biosci.* **2009**, *34*, 709–728. [\[CrossRef\]](#) [\[PubMed\]](#)

19. Chenet, A.-L.; Quidelleur, X.; Fluteau, F.; Courtillot, V.; Bajpai, S.  $^{40}\text{K}$ – $^{40}\text{Ar}$  dating of the Main Deccan large igneous province: Further evidence of KTB age and short duration. *Earth Planet. Sci. Lett.* **2007**, *263*, 1–15. [[CrossRef](#)]
20. Jay, A.; Widdowson, M. Stratigraphy, structure and volcanology of the SE Deccan continental flood basalt province: Implications for eruptive extent and volumes. *J. Geol. Soc.* **2008**, *165*, 177–188. [[CrossRef](#)]
21. Sprain, C.J.; Renne, P.R.; Vanderkluyzen, L.; Pande, K.; Self, S.; Mittal, T. The eruptive tempo of Deccan volcanism in relation to the Cretaceous-Paleogene boundary. *Science* **2019**, *363*, 866–870. [[CrossRef](#)] [[PubMed](#)]
22. Jay, A.E. Volcanic Architecture of the Deccan Traps, Western Maharashtra, India: An Integrated Chemostratigraphic and Palaeomagnetic Study. Ph.D. Thesis, The Open University, Milton Keynes, UK, 2005.
23. Beane, J.E.; Turner, C.A.; Hooper, P.R.; Subbarao, K.V.; Walsh, J.N. Stratigraphy, composition and form of the Deccan Basalts, Western Ghats, India. *Bull. Volcanol.* **1986**, *48*, 61–83. [[CrossRef](#)]
24. Hooper, P.R. The winds of change: The Deccan traps, a personal perspective. In *Deccan Volcanic Province*; Subbarao, K.V., Ed.; Memoir of the Geological Society of India: Bangalore, India, 1999.
25. Bondre, N.R.; Duraiswami, R.A.; Dole, G. A brief comparison of lava flows from the Deccan Volcanic Province and the Columbia-Oregon Plateau Flood Basalts: Implications for models of flood basalt emplacement. *J. Earth Syst. Sci.* **2004**, *113*, 809–817. [[CrossRef](#)]
26. Deshmukh, S.S. Petrographic variations in Compound flows of Deccan Traps and their significance. *GSI Mem.* **1988**, *10*, 305–319.
27. Patro, B.P.K.; Sarma, S.V.S. Trap thickness and the subtrappean structures related to mode of eruption in the Deccan Plateau of India: Results from magnetotellurics. *Earth Planets Space* **2007**, *59*, 75–81. [[CrossRef](#)]
28. Merchant, H. Structural Geology and Petrology of the Island Bombay and Surrounding Areas, Unpublished. Ph.D. Thesis, Bombay University, Mumbai, India, 1977.
29. Cripps, J.; Widdowson, M.; Spicer, R.; Jolley, D. Coastal ecosystem responses to late stage Deccan Trap volcanism: The post K–T boundary (Danian) palynofacies of Mumbai (Bombay), west India. *Palaeogeogr. Palaeoclim. Palaeoecol.* **2005**, *216*, 303–332. [[CrossRef](#)]
30. Keller, G.; Khosla, S.C.; Sharma, R.; Khosla, A. Early Danian planktic foraminifera from Cretaceous-Tertiary intertrappean beds at Jhilmili, Chhindwara District, Madhya Pradesh, India. *J. Foraminifer. Res.* **2009**, *39*, 40–55. [[CrossRef](#)]
31. Khosla, A.; Verma, O. Paleobiota from the deccan volcano-sedimentary sequences of India: Palaeoenvironments, age and paleobiogeographic implications. *Hist. Biol.* **2015**, *27*, 898–914. [[CrossRef](#)]
32. Walker, G.P.L. Some observations and interpretations on the deccan traps. *Mem. Geol. Soc. India* **1969**, *43*, 367–395.
33. Jeffery, K.L.; Henderson, P.; Subbarao, K.V.; Walsh, J.N. The zeolites of deccan basalts—A study of their distribution. In *Deccan Flood Basalts*; Subbarao, K.V., Ed.; Geological Society of India: Bangalore, India, 1988; pp. 151–162.
34. James, S.; Walsh, J.N. Zeolites from the deccan basalts: Chemistry and formation. *Mem. Geol. Soc. India* **1999**, *43*, 803–817.
35. Ottens, B. *Indien, Mineralien und Fundstellen*; Weise Verlag: München, Germany, 2011; p. 384. ISBN 978-3-921656-76-1.
36. Melluso, L.; Barbieri, M.; Beccaluva, L. Chemical evolution, petrogenesis, and regional chemical correlations of the flood basalt sequence in the central Deccan Traps, India. *J. Earth Syst. Sci.* **2004**, *113*, 587–603. [[CrossRef](#)]
37. Chenet, A.-L.; Fluteau, F.; Courtillot, V.; Gérard, M.; Subbarao, K.V. Determination of rapid Deccan eruptions across the Cretaceous-Tertiary boundary using paleomagnetic secular variation: Results from a 1200-m-thick section in the Mahabaleshwar escarpment. *J. Geophys. Res. Space Phys.* **2008**, *113*. [[CrossRef](#)]
38. Self, S.; Keszthelyi, L.; Thordarson, T. The importance of pahoehoe. *Annu. Rev. Earth Planet. Sci.* **1998**, *26*, 81–110. [[CrossRef](#)]
39. Sahagian, D.L.; Proussevitch, A.A.; Carls, W.D. Analysis of viscous basalts and lava emplacement processes for application as a palaeobarometer/paleoaltimeter. *J. Geol.* **2002**, *110*, 671–685. [[CrossRef](#)]
40. Neuser, R.D.; Bruhn, F.; Götze, J.; Habermann, D.; Richter, D.K. Kathodolumineszenz: Methodik und anwendung. *Zent. Geol. Paläontologie Part I* **1995**, *1*, 287–306.

41. Williams, A.J.; Sumner, D.Y.; Alpers, C.N.; Karunatillake, S.; Hofmann, B.A. Preserved filamentous microbial biosignatures in the Brick Flat Gossan, Iro Mountain. *Calif. Astrobiol.* **2015**, *15*, 337–668.
42. Ehrlich, H.; Rigby, J.K.; Botting, J.P.; Tsurkan, M.; Werner, C.; Schwille, P.; Petrásek, Z.; Pisera, A.; Simon, P.; Sivkov, V.; et al. Discovery of 505-million-year old chitin in the basal demosponge *Vauxia gracilenta*. *Sci. Rep.* **2013**, *3*, 17–20. [[CrossRef](#)]
43. Wysokowski, M.; Zatoń, M.; Bazhenov, V.; Behm, T.; Ehrlich, A.; Stelling, A.L.; Hog, M.; Ehrlich, H. Identification of chitin in 200-million-year-old gastropod egg capsules. *Paleobiology* **2014**, *40*, 529–540. [[CrossRef](#)]
44. Melluso, L.; Sethna, S.F. Mineral compositions in the Deccan igneous rocks of India: An overview. In *Topics in Igneous Petrology*; Ray, J., Sen, G., Ghosh, B., Eds.; Springer: Dordrecht, The Netherlands, 2011; pp. 135–139. [[CrossRef](#)]
45. Götze, J. Chemistry, textures and physical properties of quartz—Geological interpretation and technical application. *Mineral. Mag.* **2009**, *73*, 645–671. [[CrossRef](#)]
46. Sterflinger, K. Fungi as geologic agents. *Geomicrobiol. J.* **2000**, *17*, 97–124. [[CrossRef](#)]
47. Ehrlich, H.; Ilan, M.; Maldonado, M.; Muricy, G.; Bavestrello, G.; Kljajic, Z.; Carballo, J.L.; Schiaparelli, S.; Ereskovsky, A.; Schupp, P.; et al. Three-dimensional chitin-based scaffolds from Verongida sponges (Demospongiae: Porifera). Part I. Isolation and identification of chitin. *Int. J. Biol. Macromol.* **2010**, *47*, 132–140. [[CrossRef](#)]
48. Ehrlich, H.; Maldonado, M.; Spindler, K.-D.; Eckert, C.; Hanke, T.; Born, R.; Goebel, C.; Simon, P.; Heinemann, S.; Worch, H. First evidence of chitin as a component of the skeletal fibers of marine sponges. Part I. Verongidae (demospongia: Porifera). *J. Exp. Zool. Part B Mol. Dev. Evol.* **2007**, *308*, 347–356. [[CrossRef](#)]
49. Klinger, C.; Żółtowska-Aksamitowska, S.; Wysokowski, M.; Tsurkan, M.; Galli, R.; Petrenko, I.; Machałowski, T.; Ereskovsky, A.; Martinovic, R.; Muzychka, L.; et al. Express Method for Isolation of Ready-to-Use 3D Chitin Scaffolds from *Aplysina archeri* (Aplysineidae: Verongiida) Demosponge. *Mar. Drugs* **2019**, *17*, 131. [[CrossRef](#)] [[PubMed](#)]
50. Rickert, D.; Schlueter, M.; Wallmann, K. Dissolution kinetics of biogenic silica from the water column to the sediments. *Geochim. Cosmochim. Acta* **2002**, *66*, 439–455. [[CrossRef](#)]
51. Sprynskyy, M.; Pomastowski, P.; Hornowska, M.; Król, A.; Rafińska, K.; Buszewski, B. Naturally organic functionalized 3D biosilica from diatom microalgae. *Mater. Des.* **2017**, *132*, 22–29. [[CrossRef](#)]
52. Budiarti, H.A.; Puspitasari, R.N.; Hatta, A.; Sekartedjo; Risanti, D.D. Synthesis and Characterization of TiO<sub>2</sub>@SiO<sub>2</sub> and SiO<sub>2</sub>@TiO<sub>2</sub> Core-Shell Structure Using Lapindo Mud Extract via Sol-Gel Method. *Procedia Eng.* **2017**, *170*, 65–71. [[CrossRef](#)]
53. Hernandez-Ortiz, M.; Hernández-Padrón, G.; Bernal, R.; Cruz-Vázquez, C.; Castano, V. Nanocrystalline mimetic opals: Synthesis and comparative characterization vs. natural stones. *Int. J. Basic Appl. Sci.* **2015**, *4*, 238. [[CrossRef](#)]
54. Heredia, A.; Figueira, E.; Rodrigues, C.T.; Rodríguez-Galván, A.; Basiuk, V.A.; Vrieling, E.G.; Almeida, S.F. Cd<sup>2+</sup> affects the growth, hierarchical structure and peptide composition of the biosilica of the freshwater diatom *Nitzschia palea* (Kützinger) W. Smith. *Phycol. Res.* **2012**, *60*, 229–240. [[CrossRef](#)]
55. Aliabadi, M.; Shagholani, H.; Lehi, A.Y. Synthesis of a novel biocompatible nanocomposite of graphene oxide and magnetic nanoparticles for drug delivery. *Int. J. Boil. Macromol.* **2017**, *98*, 287–291. [[CrossRef](#)]
56. Di Mario, F.; Rapanà, P.; Tomati, U.; Galli, E. Chitin and chitosan from Basidiomycetes. *Int. J. Boil. Macromol.* **2008**, *43*, 8–12. [[CrossRef](#)]
57. Gupta, B.S.; Jelle, B.; Gao, T. Application of ATR-FTIR Spectroscopy to Compare the Cell Materials of Wood Decay Fungi with Wood Mould Fungi. *Int. J. Spectrosc.* **2015**, *2015*, 1–7. [[CrossRef](#)]
58. Hassainia, A.; Satha, H.; Boufi, S. Chitin from *Agaricus bisporus*: Extraction and characterization. *Int. J. Boil. Macromol.* **2018**, *117*, 1334–1342. [[CrossRef](#)]
59. Ehrlich, H.; Maldonado, M.; Parker, A.R.; Kulchin, Y.N.; Schilling, J.; Köhler, B.; Skrzypczak, U.; Simon, P.; Reiswig, H.M.; Tsurkan, M.; et al. Supercontinuum Generation in Naturally Occurring Glass Sponges Spicules. *Adv. Opt. Mater.* **2016**, *4*, 1608–1613. [[CrossRef](#)]
60. Neinhuis, C.; Nickerl, J.; Tsurkan, M.; Werner, C. The multi-layered protective cuticle of *Collembola*: A chemical analysis. *J. R. Soc. Interface* **2014**, *11*, 20140619.

61. Machałowski, T.; Wysokowski, M.; Tsurkan, M.; Galli, R.; Schimpf, C.; Rafaja, D.; Brendler, E.; Viehweger, C.; Aksamitowska, Ż.; Petrenko, I.; et al. Spider Chitin: An Ultrafast Microwave-Assisted Method for Chitin Isolation from *Caribena versicolor* Spider Molt Cuticle. *Molecules* **2019**, *24*, 3736. [[CrossRef](#)] [[PubMed](#)]
62. Ehrlich, H.; Bazhenov, V.; Debitus, C.; De Voogd, N.; Galli, R.; Tsurkan, M.; Wysokowski, M.; Meissner, H.; Bulut, E.; Kaya, M.; et al. Isolation and identification of chitin from heavy mineralized skeleton of *Suberea clavata* (Verongida: Demospongiae: Porifera) marine demosponge. *Int. J. Boil. Macromol.* **2017**, *104*, 1706–1712. [[CrossRef](#)]
63. Seyfried, W.; Bischoff, J. Low temperature basalt alteration by sea water: An experimental study at 70 °C and 150 °C. *Geochim. Cosmochim. Acta* **1979**, *43*, 1937–1947. [[CrossRef](#)]
64. Polgári, M.; Hein, J.R.; Nemeth, T.; Pál-Molnár, E.; Vigh, T. Celadonite and smectite formation in the Úrkút Mn-carbonate ore deposit (Hungary). *Sediment. Geol.* **2013**, *294*, 157–163. [[CrossRef](#)]
65. Treiman, A.H.; Morris, R.V.; Agresti, D.G.; Graff, T.G.; Achilles, C.N.; Rampe, E.B.; Bristow, T.F.; Ming, D.W.; Blake, D.F.; Vaniman, D.T.; et al. What lurks in the martian rocks and soil? Investigations of sulfates, phosphates, and perchlorates. *Am. Mineral.* **2014**, *99*, 2234–2250. [[CrossRef](#)]
66. Peretyazhko, T.; Sutter, B.; Morris, R.V.; Agresti, D.G.; Le, L.; Ming, D.W. Smectite formation from basaltic glass under acidic conditions on early Mars. *Geochim. Cosmochim. Acta* **2016**, *173*, 37–49. [[CrossRef](#)]
67. Pradeep, K.S.; Devdutt, V.U.; Vibhuti, W. Alteration of volcanic glass to well-crystallized ferrosaponite in the vesicles of the deccan trap basalts at bhuleshwar ghat section, pune district, maharashtra. *J. Geol. Soc. India* **2016**, *88*, 22–28.
68. Rykart, R. Quarz-Monographie. *Ott Verlag Thun Aufl.* **1995**, *2*, 462.
69. Lillie, R.S. The formation of structures resembling organic growths by means of electrolytic local action in metals, and the general physiological significance and control of this type of action. *Biol. Bull.* **1917**, *33*, 135–186. [[CrossRef](#)]
70. Pagano, J.J.; Thouvenel-Romans, S.; Steinbock, O. Compositional analysis of copper–silica precipitation tubes. *Phys. Chem. Chem. Phys.* **2007**, *9*, 110–116. [[CrossRef](#)]
71. Cartwright, J.H.E.; Escribano, B.; Sainz-Díaz, C.I. Chemical-Garden Formation, Morphology, and Composition. I. Effect of the Nature of the Cations. *Langmuir* **2011**, *27*, 3286–3293. [[CrossRef](#)]
72. García-Ruiz, J.M.; Kubatko, K.-A.H.; Helean, K.B.; Navrotsky, A.; Burns, P. Self-Assembled Silica-Carbonate Structures and Detection of Ancient Microfossils. *Science* **2003**, *302*, 1194–1197. [[CrossRef](#)] [[PubMed](#)]
73. García-Ruiz, J.M.; Melero-García, E.; Hyde, S.T. Morphogenesis of Self-Assembled Nanocrystalline Materials of Barium Carbonate and Silica. *Science* **2009**, *323*, 362–365. [[CrossRef](#)]
74. Satoh, H.; Tsukamoto, K.; García-Ruiz, J.M. Formation of chemical gardens on granitic rock: A new type of alteration for alkaline systems. *Eur. J. Miner.* **2014**, *26*, 415–426. [[CrossRef](#)]
75. McMahon, S. Earth’s earliest and deepest purported fossils may be iron-mineralized chemical gardens. *Proc. R. Soc. B Biol. Sci.* **2019**, *286*. [[CrossRef](#)]
76. Ehrlich, H.L. *Geomicrobiology*, 2nd ed.; Marcel Dekker: New York, NY, USA, 1990; p. 646.
77. Barns, S.M.; Nierzwicki-Bauer, S.A. Microbial diversity in ocean, surface and subsurface environments. *Rev. Mineral.* **1997**, *35*, 35–79.
78. Müller, A.; Polgári, M.; Gucsik, A.; Nagy, S.; Veres, M.; Pál-Molnár, E.; Götze, J.; Cserháti, C.; Németh, T.; Hámor-Vidó, M. Cathodoluminescent features and Raman spectroscopy of Miocene hydrothermal biomineralization embedded in cryptocrystalline silica varieties, Central Europe, Hungary. In *Micro-Raman Spectroscopy and Luminescence Studies in the Earth and Planetary Sciences*; Gucsik, A., Ed.; AIP Conference Proceedings: Melville, NY, USA, 2009.
79. Reolid, M.; Abad, I. Glauconitic laminated crusts from hydrothermal alteration of Jurassic pillow-lavas (Betic Cordillera, S Spain): A microbial influence case. *J. Iber. Geol.* **2014**, *40*, 389–408. [[CrossRef](#)]
80. Fisk, M.R.; Giovannoni, S.J.; Thorseth, I.H. Alteration of Oceanic Volcanic Glass: Textural Evidence of Microbial Activity. *Science* **1998**, *281*, 978–980. [[CrossRef](#)]
81. Furnes, H.; Staudigel, H.; Thorseth, I.H.; Torsvik, T.; Muehlenbachs, K.; Tumyr, O. Bioalteration of basaltic glass in the oceanic crust. *Geochem. Geophys. Geosystems* **2001**, *2*, 8. [[CrossRef](#)]
82. Furnes, H.; Banerjee, N.R.; Muehlenbachs, K.; Staudigel, H.; De Wit, M.J. Early Life Recorded in Archean Pillow Lavas. *Science* **2004**, *304*, 578–581. [[CrossRef](#)]
83. Banerjee, N.R.; Muehlenbachs, K. Tuff life: Bioalteration in volcanoclastic rocks from the Ontong Java Plateau. *Geochem. Geophys. Geosystems* **2003**, *4*, 4. [[CrossRef](#)]

84. Benzerara, K.; Menguy, N.; Banerjee, N.; Tylliszczak, T.; Brown, G.; Guyot, F. Alteration of submarine basaltic glass from the Ontong Java Plateau: A STXM and TEM study. *Earth Planet. Sci. Lett.* **2007**, *260*, 187–200. [[CrossRef](#)]
85. Crovisier, J.; Honnorez, J.; Eberhart, J. Dissolution of basaltic glass in seawater: Mechanism and rate. *Geochim. Cosmochim. Acta* **1987**, *51*, 2977–2990. [[CrossRef](#)]
86. Fisk, M.R.; Crovisier, J.-L.; Honnorez, J. Experimental abiotic alteration of igneous and manufactured glasses. *Comptes Rendus Geosci.* **2013**, *345*, 176–184. [[CrossRef](#)]
87. Ivarsson, M.; Lausmaa, J.; Lindblom, S.; Broman, C.; Holm, N. Fossilized Microorganisms from the Emperor Seamounts: Implications for the Search for a Subsurface Fossil Record on Earth and Mars. *Astrobiology* **2008**, *8*, 1139–1157. [[CrossRef](#)]
88. Fernández-Remolar, D.; Prieto-Ballesteros, O.; Rodríguez, N.; Gomez, F.; Amils, R.; Gómez-Elvira, J.; Stoker, C.R. Underground Habitats in the Río Tinto Basin: A Model for Subsurface Life Habitats on Mars. *Astrobiology* **2008**, *8*, 1023–1047. [[CrossRef](#)]
89. Williams, A.J.; Alpers, C.N.; Sumner, D.Y.; Campbell, K.M. Filamentous Hydrous Ferric Oxide Biosignatures in a Pipeline Carrying Acid Mine Drainage at Iron Mountain Mine, California. *Geomicrobiol. J.* **2016**, *34*, 193–206. [[CrossRef](#)]
90. Kretzschmar, M. Fossile Pilze in Eisen-Stromatolithen von Warstein (Rheinisches Schiefergebirge). *Facies* **1982**, *7*, 237–259. [[CrossRef](#)]
91. Baele, J.-M.; Boulvain, F.; Jong, J.D.; Matielli, N.; Papier, S.; Pr at, A. Iron microbial mats in Modern and Phanerozoic environments. In *Instruments, Methods, and Missions for Astrobiology*; Hoover, R.B., Levin, G.V., Rozanov, A.Y., Davies, P.C.W., Eds.; XI, Proceedings of SPIE: Bellingham, WA, USA, 2008.
92. Zhou, X.; Chen, D.; Tang, D.; Dong, S.; Guo, C.; Guo, Z.; Zhang, Y. Biogenic Iron-Rich Filaments in the Quartz Veins in the Uppermost Ediacaran Qigebulake Formation, Aksu Area, Northwestern Tarim Basin, China: Implications for Iron Oxidizers in Subseafloor Hydrothermal Systems. *Astrobiology* **2015**, *15*, 523–537. [[CrossRef](#)] [[PubMed](#)]
93. Reysenbach, A.L.; Cady, S.L. Microbiology of ancient and modern hydrothermal systems. *Trends Microbiol.* **2001**, *9*, 79–86. [[CrossRef](#)]
94. Cartwright, J.H.E.; Garc a-Ruiz, J.M.; Novella, M.L.; Ot alora, F. Formation of chemical gardens. *J. Colloid Interface Sci.* **2002**, *256*, 351–359. [[CrossRef](#)]
95. Barge, L.M.; Cardoso, S.S.S.; Cartwright, J.H.E.; Cooper, G.J.T.; Cronin, L.; De Wit, A.; Doloboff, I.J.; Escribano, B.; Goldstein, E.R.; Haudin, F.; et al. From Chemical Gardens to Chemobionics. *Chem. Rev.* **2015**, *115*, 8652–8703. [[CrossRef](#)] [[PubMed](#)]
96. Kellermeier, M.; C olfen, H.; Garc a-Ruiz, J.M. Silica Biomorphs: Complex Biomimetic Hybrid Materials from “Sand and Chalk”. *Eur. J. Inorg. Chem.* **2012**, *2012*, 5123–5144. [[CrossRef](#)]
97. Krepski, S.T.; Emerson, D.; Hredzak-Showalter, P.L.; Luther, G.W.; Chan, C.S. Morphology of biogenic iron oxides records microbial physiology and environmental conditions: Toward interpreting iron microfossils. *Geobiology* **2013**, *11*, 457–471. [[CrossRef](#)]
98. Johannessen, K.C.; McLoughlin, N.; Vullum, P.E.; Thorseth, I.H. On the biogenicity of Fe-oxyhydroxide filaments in silicified low-temperature hydrothermal deposits: Implications for the identification of Fe-oxidizing bacteria in the rock record. *Geobiology* **2019**, *18*, 31–53. [[CrossRef](#)]
99. Perry, R.S.; McLoughlin, N.; Lynne, B.Y.; Sephton, M.; Oliver, J.D.; Perry, C.C.; Campbell, K.A.; Engel, M.H.; Farmer, J.D.; Brasier, M.D.; et al. Defining biominerals and organominerals: Direct and indirect indicators of life. *Sediment. Geol.* **2007**, *201*, 157–179. [[CrossRef](#)]
100. Oggerin, M.; Rodriguez, N.; Del Moral, C.; Amils, R. Fungal jarosite biomineralization in R o Tinto. *Res. Microbiol.* **2014**, *165*, 719–725. [[CrossRef](#)]
101. Li, H.; Hu, S.; Polizzotto, M.L.; Chang, X.; Shen, Q.; Ran, W.; Yu, G.-H. Fungal biomineralization of montmorillonite and goethite to short-range-ordered minerals. *Geochim. Cosmochim. Acta* **2016**, *191*, 17–31. [[CrossRef](#)]
102. Bindschedler, S.; Cailleau, G.; Verrecchia, E.P. Role of Fungi in the Biomineralization of Calcite. *Minerals* **2016**, *6*, 41. [[CrossRef](#)]
103. Mistri, A.; Quirin, M.E.C.; Mukherjee, A. Carbonate biomineralization and heavy metal remediation by calcifying fungi isolated from karstic caves. *Ecol. Eng.* **2017**, *103*, 106–117.

104. Tazaki, K. Clays, microorganisms, and biomineralization. In *Handbook of Clay Science*; Bergaya, F., Theng, B.K.G., Lagaly, G., Eds.; Elsevier: Amsterdam, The Netherlands, 2006; pp. 477–497.
105. Köhler, B.; Singer, A.; Stoffers, P. Biogenic nontronite from marine white smoker chimneys. *Clays Clay Miner.* **1994**, *42*, 689–701. [[CrossRef](#)]
106. Ueshima, M.; Tazaki, K. Possible role of microbial polysaccharides in nontronite formation. *Clays Clay Miner.* **2001**, *49*, 292–299. [[CrossRef](#)]
107. Schultze-Lam, S.; Fortin, D.; Davis, B.S.; Beveridge, T.J. Mineralization of bacterial surfaces. *Chem. Geol.* **1996**, *132*, 171–181. [[CrossRef](#)]
108. Kawano, M.; Tomita, K. Microbiotic formation of silicate minerals in the weathering environment of a pyroclastic deposit. *Clays Clay Miner.* **2002**, *50*, 99–110. [[CrossRef](#)]
109. Ferris, F.G.; Beveridge, T.J.; Fyfe, W.S. Iron-silica crystallite nucleation by bacteria in a geothermal sediment. *Nature* **1986**, *320*, 609–611. [[CrossRef](#)]
110. Konhauser, K.O.; Urrutia, M.M. Bacterial clay authigenesis: A common biogeochemical process. *Chem. Geol.* **1999**, *161*, 399–413. [[CrossRef](#)]
111. Urrutia, M.M.; Beveridge, T.J. Formation of fine-grained meal and silicate precipitates on abacterial surface (*Bacillus subtilis*). *Chem. Geol.* **1994**, *116*, 261–280. [[CrossRef](#)]
112. Skinner, H.C.W.; Jahren, A.H. Biomineralization. In *Treatise on Geochemistry*; Elsevier: Amsterdam, The Netherlands, 2003; pp. 117–184.
113. Melton, E.D.; Swanner, E.D.; Behrens, S.; Schmidt, C.; Kappler, A. The interplay of microbially mediated and abiotic reactions in the biogeochemical Fe cycle. *Nat. Reviews Microbiol.* **2014**, *12*, 797–808. [[CrossRef](#)]
114. Chan, C.S.; De Stasio, G.; Welch, S.A.; Girasole, M.; Frazer, B.H.; Nesterova, M.V.; Fakra, S.; Banfield, J.F. Microbial saccharides template assembly of nanocrystal fibres. *Science* **2004**, *303*, 1656–1658. [[CrossRef](#)] [[PubMed](#)]
115. Tazaki, K. Biomineralization of layer silicates and hydrated Fe/Mn Oxides in Microbial Mats: An Electron Microscopical Study. *Clays Clay Miner.* **1997**, *45*, 203–212. [[CrossRef](#)]
116. Konhauser, K.O. Diversity of bacterial iron mineralization. *Earth Sci. Rev.* **1998**, *43*, 91–121. [[CrossRef](#)]



© 2020 by the authors. Licensee MDPI, Basel, Switzerland. This article is an open access article distributed under the terms and conditions of the Creative Commons Attribution (CC BY) license (<http://creativecommons.org/licenses/by/4.0/>).